The Lipogenic Regulator SREBP2 Induces Transferrin in Circulating Melanoma Cells and Suppresses Ferroptosis

Xin Hong[1], Whijae Roh[2], Ryan J. Sullivan[1,3], Keith H.K. Wong[4,5], Ben S. Wittner[1], Hongshan Guo[1], Taronish D. Dubash[1], Moshe Sade-Feldman[1,2], Benjamin Wesley[1], Elad Horwitz[1], Genevieve M. Boland[1,6], Dieuwke L. Marvin[1], Todd Bonesteel[1], Chenyue Lu[1], François Aguet[2], Risa Burr[1], Samuel S. Freeman[2], Laxmi Parida[9], Katherine Calhoun[1,4], Michelle K. Jewett[1,4], Linda T. Nieman[1], Nir Hacohen[1,2], Anders M. Näär[1], David T. Ting[1,3], Mehmet Toner[4,5,6], Shannon L. Stott[1,3], Gad Getz[1,2,7], Shyamala Maheswaran[1,6], and Daniel A. Haber[1,3,8]

ABSTRACT

Circulating tumor cells (CTC) are shed by cancer into the bloodstream, where a viable subset overcomes oxidative stress to initiate metastasis. We show that single CTCs from patients with melanoma coordinately upregulate lipogenesis and iron homeostasis pathways. These are correlated with both intrinsic and acquired resistance to BRAF inhibitors across clonal cultures of *BRAF*-mutant CTCs. The lipogenesis regulator SREBP2 directly induces transcription of the iron carrier Transferrin (*TF*), reducing intracellular iron pools, reactive oxygen species, and lipid peroxidation, thereby conferring resistance to inducers of ferroptosis. Knockdown of endogenous *TF* impairs tumor formation by melanoma CTCs, and their tumorigenic defects are partially rescued by the lipophilic antioxidants ferrostatin-1 and vitamin E. In a prospective melanoma cohort, presence of CTCs with high lipogenic and iron metabolic RNA signatures is correlated with adverse clinical outcome, irrespective of treatment regimen. Thus, SREBP2-driven iron homeostatic pathways contribute to cancer progression, drug resistance, and metastasis.

SIGNIFICANCE: Through single-cell analysis of primary and cultured melanoma CTCs, we have uncovered intrinsic cancer cell heterogeneity within lipogenic and iron homeostatic pathways that modulates resistance to BRAF inhibitors and to ferroptosis inducers. Activation of these pathways within CTCs is correlated with adverse clinical outcome, pointing to therapeutic opportunities.

[1]Massachusetts General Hospital Cancer Center and Harvard Medical School, Boston, Massachusetts. [2]Broad Institute of Harvard and MIT, Cambridge, Massachusetts. [3]Department of Medicine, Massachusetts General Hospital and Harvard Medical School, Boston, Massachusetts. [4]Center for Engineering in Medicine, Department of Surgery, Massachusetts General Hospital and Harvard Medical School, Boston, Massachusetts. [5]Shriners Hospitals for Children, Boston, Massachusetts. [6]Department of Surgery, Massachusetts General Hospital and Harvard Medical School, Boston, Massachusetts. [7]Department of Pathology, Massachusetts General Hospital and Harvard Medical School, Boston, Massachusetts. [8]Howard Hughes Medical Institute, Bethesda, Maryland. [9]IBM Research, Yorktown Heights, New York.

Note: Supplementary data for this article are available at Cancer Discovery Online (http://cancerdiscovery.aacrjournals.org/).

X. Hong and W. Roh contributed equally to this article.

Current address for X. Hong: School of Medicine, Southern University of Science and Technology, Shen Zhen, China; and current address for A.M. Näär, Department of Nutritional Sciences and Toxicology, University of California, Berkeley, California.

Corresponding Authors: Daniel A. Haber, MGH Cancer Center, Building 149, 13th Street, Charlestown, MA 02129. Phone: 617-726-7805; E-mail: dhaber@mgh.harvard.edu; and Shyamala Maheswaran, maheswaran@helix.mgh.harvard.edu

Cancer Discov 2021;11:678–95

doi: 10.1158/2159-8290.CD-19-1500

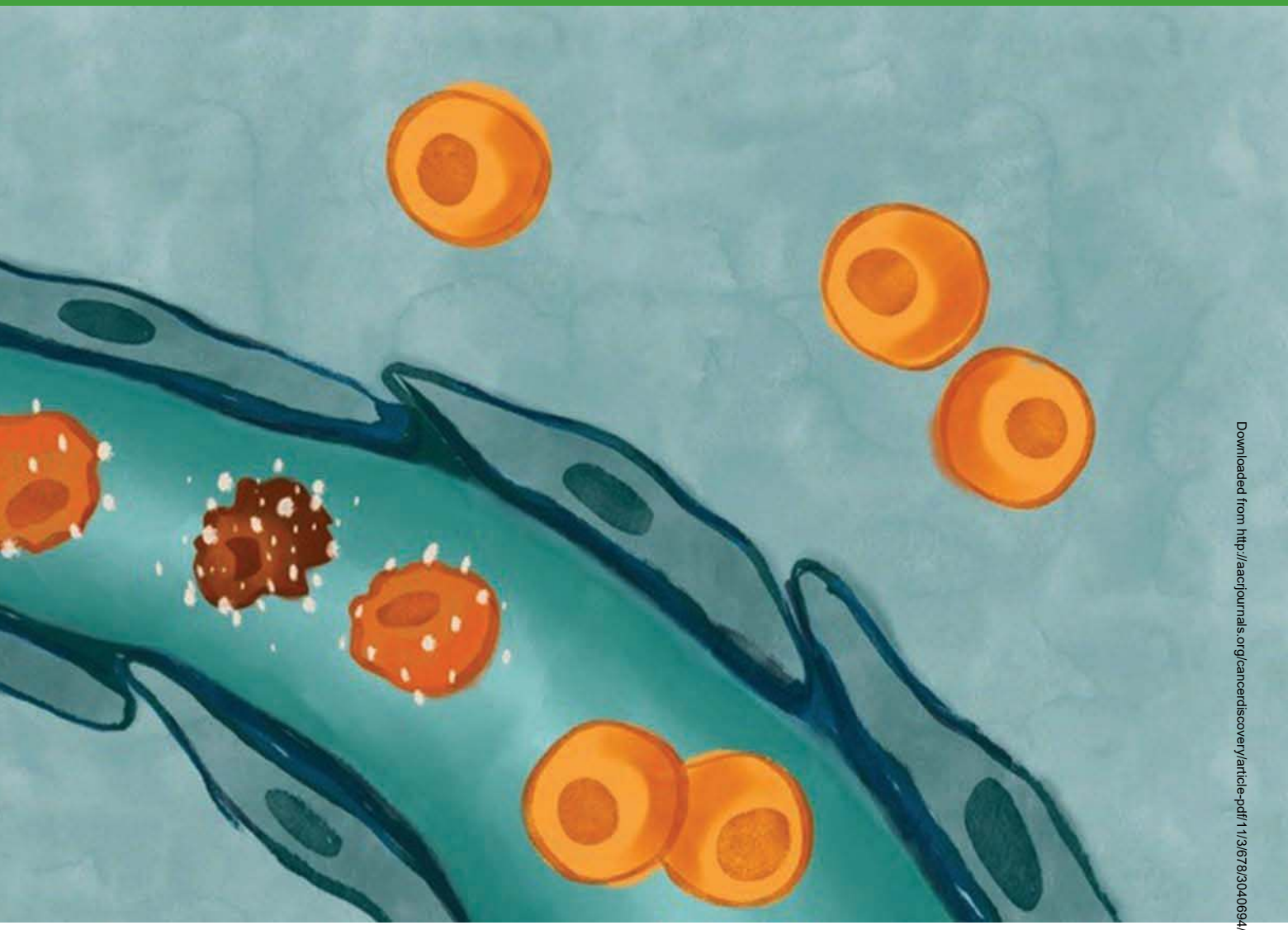

INTRODUCTION

Metastatic melanoma remains a highly lethal malignancy, despite breakthroughs in the targeted treatment of *BRAF*-mutant cases (1–3) and the application of immune checkpoint therapies irrespective of genotype (4–8). Melanomas with $BRAF^{V600E}$ and associated oncogenic variants typically undergo rapid tumor shrinkage following treatment with combination BRAF and MEK inhibitors, although there is considerable variation in the degree of initial response, and virtually all cases recur with drug-resistant disease. The effectiveness of immune-targeted therapies appears to be determined in part by total mutational burden in the tumor and the associated presentation of neoantigens, which are typically high in melanoma (9–14), but only a third of patients have sustained responses (15, 16). For both targeted and immune-based therapies, innate and acquired resistance is compounded by tumor heterogeneity in signaling pathways, expression of cell surface epitopes, and intrinsic cell survival pathways.

The transition from primary melanoma to metastatic disease is characterized by blood-based dissemination of circulating tumor cells (CTC) to diverse metastatic sites, as is the progression from oligometastatic to widespread metastatic disease. Although melanoma cells are notoriously invasive and resistant to any therapeutic interventions other than immunologic and BRAF-targeted treatments, the exceptional environment in the bloodstream may provide new therapeutic opportunities to suppress metastasis.

Specifically, the high oxygen content of blood has been shown to render primary melanoma cells vulnerable to reactive oxygen species (ROS; ref. 17). Identifying innate mechanisms that confer resistance to ROS, and thereby enable a subset of melanoma cells to remain viable as they circulate in the blood, may thus provide new therapeutic targets to suppress metastatic precursors.

The small number of CTCs present within a blood specimen, admixed to billions of normal blood cells, presents significant technical challenges to their isolation and functional analysis (18). Neural crest–derived melanoma cells do not express the epithelial cell surface protein epithelial cell adhesion molecule EPCAM, which is traditionally used to capture CTCs using magnetically conjugated antibody

enrichment (19, 20). Furthermore, melanoma cells display a high degree of heterogeneity in cell surface epitope expression, which complicates their direct capture using lineage- or tumor-specific antibody panels (21). In designing a tumor-agnostic strategy for isolating CTCs within blood specimens, we developed a platform (CTC-iChip) for efficient depletion of normal blood cells, thereby enriching for cancer cells irrespective of cell surface markers (22, 23). Taking advantage of microfluidic flow kinetics, this CTC-iChip achieves initial size-based exclusion of red blood cells and platelets, followed by inertial focusing of all nucleated blood cells into a single streamline, through which antibody-tagged leukocytes are magnetically separated from unlabeled CTCs. Across multiple tumor types, this platform achieves 10^4 enrichment for CTCs, and we have applied a digital RNA-based readout to allow highly sensitive measurement of melanoma tumor cell burden in the blood (24). The enrichment of untagged and unmanipulated CTCs not only enhances their RNA quality for such diagnostic purposes, but also helps to preserve their cell viability for functional studies.

We have previously reported the establishment of long-term CTC cultures from blood specimens of women with hormone receptor–positive breast cancer, which are often oligoclonal in origin and which recapitulate somatic mutations acquired during the course of therapy, and their epigenetic cell states (25–27). Here, we established CTC cultures from blood samples of patients with metastatic melanoma, comparing their transcriptomes across different cases, as well as in multiple single CTC-derived isogenic lines from the same patient. In these cultured melanoma CTCs and in single CTCs freshly isolated from blood specimens, we find striking upregulation of SREBP-driven lipogenic pathways, together with iron homeostatic pathways, including the iron transport protein Transferrin (*TF*). The master regulator of cholesterol homeostasis SREBP2, encoded by the *SREBF2* gene, directly induces expression of *TF*, which in turn suppresses ROS and drug-induced ferroptotic cell death. Modulating these pathways in mouse models has a dramatic effect on metastasis, whereas their overexpression within patient-derived CTCs is strongly correlated with an adverse clinical outcome. Thus, the coordinated overexpression of SREBP target genes and *TF* in melanoma CTCs points to a regulatory pathway linking lipogenesis with iron homeostasis, contributing to the ability of viable CTCs to overcome oxidative damage in the circulation.

RESULTS

Melanoma Patient–Derived Tumorigenic CTC Cultures Overexpress Lipogenic and Iron Homeostatic Pathways

We generated patient-derived CTC cultures following microfluidic enrichment from blood samples of patients with metastatic melanoma. Five independent cultures were established from four patients [out of a cohort of 37 patients undergoing treatment on Institutional Review Board (IRB)–approved protocols at Massachusetts General Hospital Cancer Center]. The CTC-iChip was used to deplete normal hematopoietic cells from 10 mL of whole blood, and the enriched, unlabeled CTCs were maintained in anchorage-independent media, under hypoxic conditions, and in the presence of heparin and RHO kinase inhibitor (refs. 22, 23, 25; see Methods). To confirm their identity as melanoma cells, the cultured CTCs were tested for expression of characteristic melanoma markers (ref. 24; Fig. 1A; Supplementary Fig. S1A and S1B) and shown to have shared mutational profiles with their respective parental tumors, including the canonical drug-sensitizing $BRAF^{V600E}$ or $NRAS^{Q61K}$ mutations, as well as displaying predicted BRAF and MEK inhibitor sensitivity patterns (Fig. 1A; Supplementary Fig. S1C and S1D). The melanoma CTC lines were tested for tumorigenesis potential in immunosuppressed NOD/SCID gamma (NSG) mice. All five cultured lines are highly tumorigenic following subcutaneous inoculation, and four of them (PEM-78 being the exception) generated metastases upon direct intravascular injection, either by tail-vein or intracardiac inoculation (Fig. 1B and C; Supplementary Fig. S1E–S1J). Both primary tumors and metastases generated from GFP-luciferase–tagged CTCs show preservation of characteristic melanosome markers (Fig. 1C; Supplementary Fig. S1F, S1H, and S1K). We selected two of these CTC lines, Mel-167 and Mel-182-2, for detailed functional studies.

Having established robust tumorigenic and metastatic competent CTC cultures, we compared their transcriptomic profiles with those of standard melanoma tumor–derived cell lines [Cancer Cell Line Encyclopedia (CCLE)] and primary and metastatic melanoma tumors [The Cancer Genome Atlas (TCGA); refs. 28, 29]. By gene set variation analysis (GSVA; ref. 30), we found that the most significantly enriched pathways in the CTC lines were those involved in lipogenesis ("SREBP_TARGET," "FATTY_ACID_METABOLISM," "ADIPOGENESIS," and "CHOLESTEROL_HOMEOSTASIS"), along with iron-related pathways, including "OXIDATIVE_PHOSPHORYLATION," "FERROPTOSIS," and "IRON_ION_HOMEOSTASIS," after correction for batch effect (Fig. 1D–F; Supplementary Fig. S2A and S2B). The dramatic enrichment of multiple pathways in CTC lines appears to be independent of tumor site of origin or differences in culture media and hypoxic conditions *in vitro*. A modest increase in SREBP_TARGET signatures is also observed in CCLE cell lines when compared with primary tumor samples (Fig. 1D; Supplementary Tables S1–S3). Thus, transcriptional profiling of cultured melanoma CTC lines from multiple patients compared with traditional melanoma cell lines and with primary melanoma specimens reveals concurrent upregulation of lipogenesis and iron-dependent metabolic signatures.

Single Cell–Derived CTC Cultures Exhibit Innate Resistance to BRAF Inhibition through Enhanced Lipogenesis

Mel-167 CTC cultures, established prior to any treatment administration from a patient who was newly diagnosed with metastatic melanoma, are multiclonal in origin. Despite having the characteristic $BRAF^{V600E}$ drug-sensitizing mutation, the patient had only a transient (<3 months) clinical response to the standard combined BRAF/MEK inhibition regimen, suggesting the presence of intrinsically drug-resistant cancer cells at the time of diagnosis. Upon generating 13 single CTC-derived clones from the pretreatment specimen, we indeed observed a range of sensitivity to the BRAF inhibitor vemurafenib

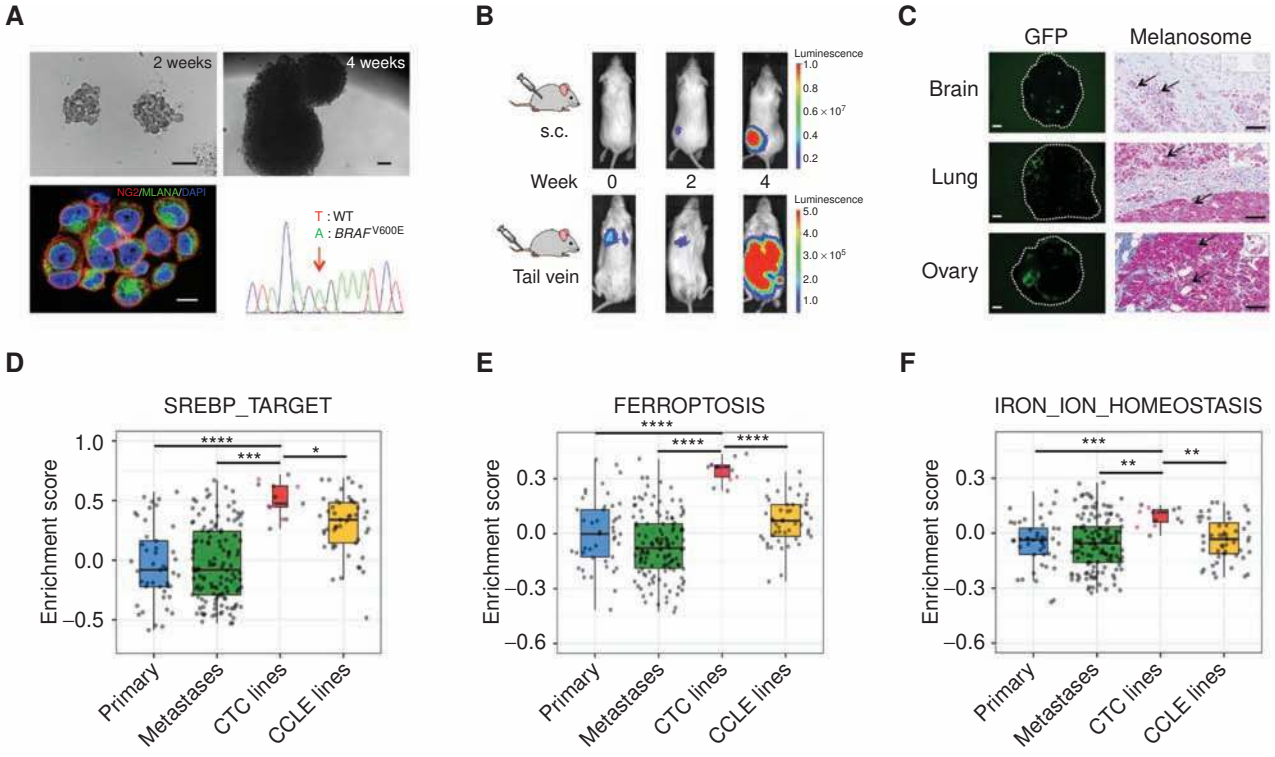

Figure 1. Lipogenic and iron homeostasis signatures are elevated in CTC lines derived from patients with melanoma. **A,** Characterization of *ex vivo* cultures of melanoma Mel-167 CTCs. Top, brightfield images of suspension cultures at 2 weeks (left; scale bar, 100 μm) and 4 weeks (right; scale bar, 100 μm). Bottom left, Representative immunofluorescence image of cultured CTCs costained for melanoma markers NG2 (red) and MLANA (green), with nuclear DAPI (blue). DAPI, 4′,6-diamidino-2-phenylindole. Scale bar, 10 μm. Bottom right, DNA sequencing identifies the heterozygous *BRAF*^{V600E} mutation (T→ A at nucleotide 1799) in the cultured melanoma Mel-167 CTCs. WT, wild type. **B,** Melanoma Mel-167 CTCs are tumorigenic in mice. Primary tumors (top) and metastases (bottom) following s.c. and tail-vein injection in NSG mice, respectively, of GFP-luciferase–tagged Mel-167 CTCs, monitored over 4 weeks using IVIS. **C,** Intracardiac inoculation of GFP-luciferase–tagged Mel-167 CTCs into NSG mice leading to metastases in brain, lung, and ovary. Representative images of GFP-expressing tumor cells in tissue sections (left plots, hatched circles; scale bar, 2 mm) and immunohistochemical staining for melanosomes (right plots, purple stain of individual melanoma cells marked by black arrows, with whole tissue section shown on the top right box; scale bar, 100 μm). **D-F,** GSVA pathway enrichment box plots of (**D**) SREBP_TARGET, (**E**) FERROPTOSIS, and (**F**) IRON_ION_HOMEOSTASIS, comparing melanoma CTC cell line samples ($n = 13$, including 5 distinct lines colored in pink and 8 sample repeats of these 5 lines in gray) with TCGA high-purity primary melanomas ($n = 45$; Primary), TCGA high-purity metastatic melanomas ($n = 129$; Metastases) and CCLE melanoma cell lines ($n = 49$). The mean GSVA enrichment scores were calculated for replicates of each CTC line. Pairwise comparisons between CTC lines and the other three categories were performed, and statistical significance was assessed by two-sided Welch *t* test (*, $P < 0.05$; **, $P < 0.01$; ***, $P < 0.001$; ****, $P < 0.0001$). Curated pathway signature gene lists are found in Supplementary Table S2.

among these untreated cultured CTC clones (Fig. 2A and B). Defining the resistant versus sensitive clones as those with an IC_{50} for vemurafenib that is either above or below that of the bulk CTC population, we first tested for mutational heterogeneity using whole-exome sequencing (WES) of four resistant clonal lines, versus two sensitive clones, the bulk parental Mel-167 culture, and the matched primary melanoma tumor (Supplementary Fig. S3A). No new driver mutations were detected across these clonally related lines that could account for the differential drug sensitivity. However, RNA sequencing (RNA-seq) profiles of all 13 isogenic CTC lines, followed by GSVA, identified lipogenesis pathways as being highly enriched in the drug-resistant CTC clones, compared with sensitive lines (CHOLESTEROL_HOMEOSTATIS, $P = 0.0098$; SREBF1_TARGET, $P = 0.0135$; SREBF2_TARGET, $P = 0.0212$; and SREBP_TARGET, $P = 0.0201$; Fig. 2C; Supplementary Fig. S3B). The individual clones were heterogeneous with respect to tumorigenic phenotypes (Supplementary Fig. S3C). Thus, upregulation of SREBP-dependent lipogenesis is correlated with innate resistance to BRAF inhibition, within a subset of untreated patient-derived isogenic clonal CTC lines.

To test the functional consequences of modulating SREBP activity in these untreated cultured melanoma CTCs, we achieved double knockdown of *SREBF1* and *SREBF2* using siRNA combinations in parental Mel-167 CTCs, showing significant enhancement of sensitivity to the BRAF inhibitor vemurafenib (Fig. 2D; Supplementary Fig. S3D). Conversely, doxycycline-inducible expression of a mature isoform of SREBP2, which bypasses normal cellular processing and directly translocates to the nucleus to activate lipogenic signaling (31), results in a high degree of resistance to vemurafenib (Fig. 2E). We also tested the effect of the SREBP inhibitor fatostatin: Mel-167 CTCs display strong cooperative sensitivity to vemurafenib and fatostatin in suppressing soft-agar colony number (Fig. 2F) and soft-agar colony size (Supplementary Fig. S3E), established *in vitro* correlates of tumorigenicity.

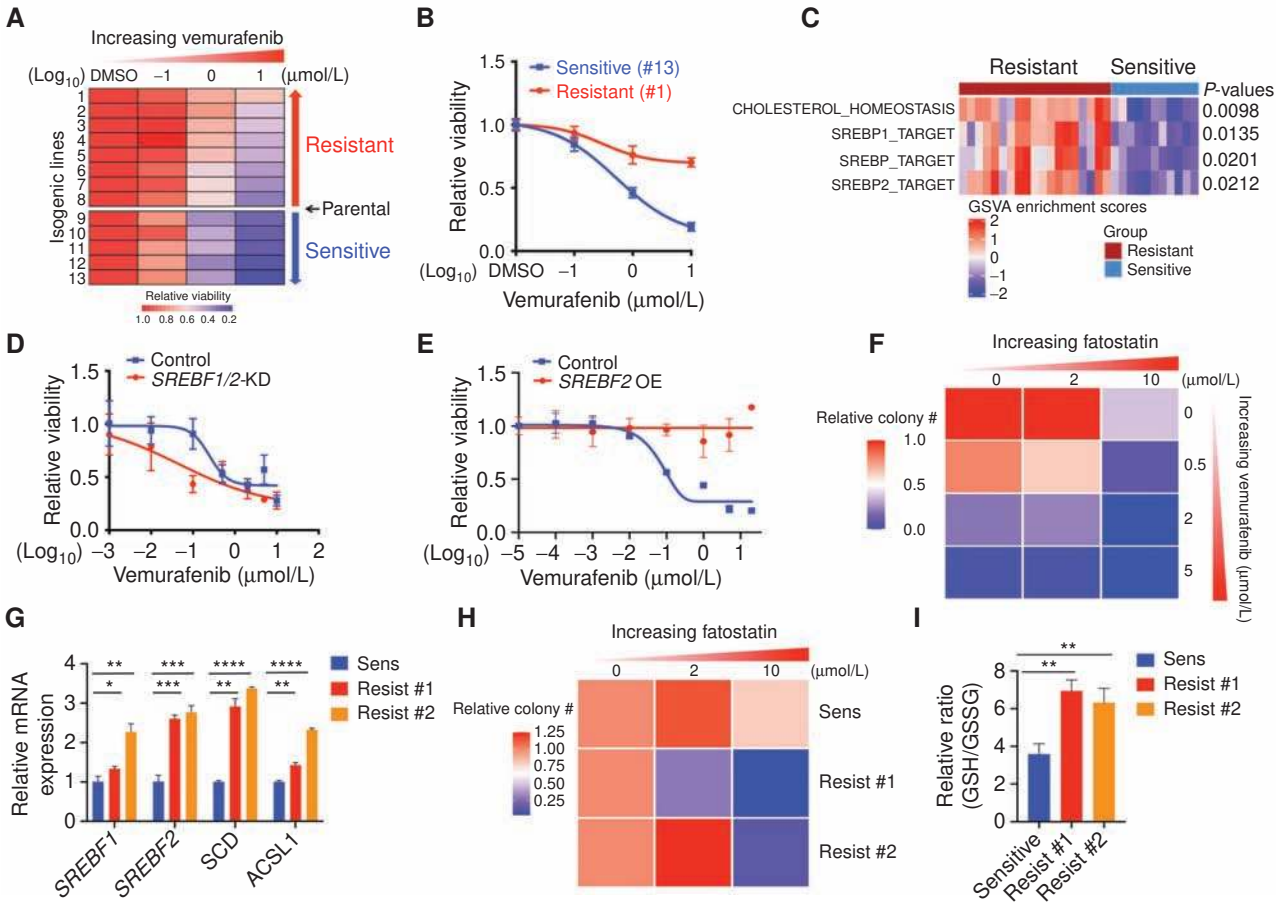

Figure 2. Clonal heterogeneity in SREBP-dependent lipogenesis as a mediator of intrinsic resistance to BRAF inhibitor among melanoma CTCs. **A,** Heat map of BRAF inhibitor (BRAFi; vemurafenib) drug sensitivity performed on 13 single CTC-derived isogenic clones derived from one pretreatment blood sample from patient Mel-167 (tumor is *BRAF*^{V600E}-positive). Rows, left to right, relative cell viability with increasing vemurafenib concentrations: 0 (DMSO control), 0.1, 1, and 10 μmol/L. Columns, top to bottom, isogenic CTC lines ranked from lowest to highest sensitivity to BRAFi. The 13 isogenic lines are divided into sensitive ($n = 5$) versus resistant ($n = 8$) groups based on their BRAFi sensitivity compared with the uncloned parental CTC culture. The isogenic lines have virtually identical mutational profiles compared with the primary tumor specimen, the parental Mel-167 CTC culture, and with each other (refer to Supplementary Fig. S3A). **B,** Vemurafenib sensitivity curves of two representative isogenic melanoma CTC lines, #1 (sensitive, blue line) and #13 (resistant, red line). *y*-axis, relative cell viability; *x*-axis, drug concentrations in $\log_{10}$ scale. Statistical significance is assessed by two-sided *t* test with unequal variance when comparing differences in cell viabilities between line #1 and line #13 treated with vemurafenib at different concentrations: $P = 0.0009$ (1 μmol/L) and $P = 7.56 \times 10^{-7}$ (10 μmol/L). **C,** Heat map showing GSVA enrichment scores of pathways that were significantly different between BRAFi-sensitive (blue) and BRAFi-resistant (red) isogenic CTC lines. The statistical significance was defined as the gene sets with FDR-adjusted *P* values < 0.05 and absolute mean difference in GSVA scores between two groups > 0.25. *P* values were assessed by the two-sided Welch *t* test. The heat map for all pathways is shown in Supplementary Fig. S3B. **D,** Vemurafenib sensitivity of the *BRAF*^{V600E}-mutant CTCs following depletion of *SREBF1* and *SREBF2* using siRNAs, compared with cells treated with control. *y*-axis, relative viability; *x*-axis, drug concentration in μmol/L, $\log_{10}$ scale. The knockdown efficiency against *SREBF1* and *SREBF2* is shown in Supplementary Fig. S3C. Statistical significance is assessed by two-sided *t* test with unequal variance. $P = 0.0121$ when comparing differences in cell viabilities between control and *SREBF1/2*-KD groups treated with 0.1 μmol/L vemurafenib. **E,** Vemurafenib sensitivity of the *BRAF*^{V600E}-mutant CTCs with ectopic expression of a mature and activated form of *SREBF2*. Vector-transfected cells are shown as controls. *y*-axis, relative viability; *x*-axis, drug concentration in μmol/L, $\log_{10}$ scale. The mRNA and protein level of *SREBF2* overexpression (OE) is shown in Fig. 3H and I, respectively. Statistical significance is assessed by two-sided *t* test with unequal variance, and *P* values are generated when comparing cell viabilities between control and *SREBF2* OE groups treated with vemurafenib at different concentrations: $P = 0.0022$ (0.1 μmol/L); $P = 0.0417$ (1 μmol/L); $P = 0.0126$ (5 μmol/L); $P = 2.11 \times 10^{-6}$ (20 μmol/L). **F,** Heat map representing soft-agar colony numbers following treatment of Mel-167 CTCs with increasing concentrations of the BRAFi vemurafenib and SREBP inhibitor fatostatin, which show cooperative cell toxicity. The drug effect on colony size is shown in Supplementary Fig. S3E. **G,** Elevated expression of *SREBF1*, *SREBF2*, and their downstream targets SCD and ACSL1 in parental Mel-167 CTC cultures (sensitive) and in two clones with acquired resistance to vemurafenib (clones #1 and #2). *y*-axis, relative fold change of mRNAs (qRT-PCR) shown between sensitive parental and the resistant lines (Actin internal control). Data were obtained from three biological repeats. Statistical significance is assessed by two-sided *t* test with unequal variance. For comparing sample Resist #1 to Sens ($P = 0.0374$ for SREBF1; $P = 0.0005$ for SREBF2; $P = 0.0030$ for SCD; $P = 0.0016$ for ACSL1); for comparing Resist #2 to Sens ($P = 0.0018$ for SREBF1; $P = 0.0002$ for SREBF2; $P < 0.0001$ for SCD; $P < 0.0001$ for ACSL1). *, $P < 0.05$; **, $P < 0.01$; ***, $P < 0.001$; ****, $P < 0.0001$. **H,** Heat map representing soft-agar clonogenic ability of the parental (sensitive) Mel-167 CTCs, compared with two vemurafenib-resistant derivative clones (#1 and #2), following treatment with increasing concentrations of the SREBP inhibitor fatostatin. The vemurafenib-resistant CTCs show increased sensitivity to fatostatin. Statistical significance was assessed by two-sided *t* test with Welch correction ($P = 0.0168$, comparing resistant clone #1 with sensitive line; $P = 0.0139$ comparing resistant clone #2 with sensitive line). The drug effect on colony size is shown in Supplementary Fig. S3F. **I,** Increased ratio of GSH to GSSG, indicative of enhanced reductive capacity, in two Mel-167-CTC clonal lines with acquired resistance to vemurafenib compared with the control-sensitive cells. Statistical significance was assessed by two-sided *t* test with Welch correction. $P = 0.0020$, comparing Resist #1 with Sensitive line, and $P = 0.0092$, comparing Resist #2 with Sensitive line (**, $P < 0.01$).

To test whether the effect of SREBP-dependent lipogenesis extends from innate resistance to vemurafenib in untreated melanoma cells to acquired drug-induced resistance, we cultured Mel-167 CTCs in the presence of 1 μmol/L vemurafenib for 3 months, generating two independent resistant CTC lines. In both resistant lines, we find a significant increase in expression of endogenous *SREBF1* and *SREBF2*, along with increased expression of the SREBP target genes *SCD* and *ACSL1* (Fig. 2G). Both Mel-167 CTC lines with acquired vemurafenib resistance display enhanced sensitivity to the SREBP inhibitor fatostatin, as measured by reduced number and size of soft-agar colonies (Fig. 2H; Supplementary Fig. S3F). Finally, consistent with an effect of lipogenic regulation on cellular redox potential, both SREBP-high, vemurafenib-resistant Mel-167 clones show an increased reduced-to-oxidized glutathione (GSH/GSSG) ratio, indicative of enhanced ROS-neutralizing capacity (Fig. 2I; total GSH and GSSG levels are shown in Supplementary Fig. S3G and S3H).

Taken together, resistance by *BRAF*-mutant CTCs to vemurafenib is correlated with SREBP activity, both among heterogeneous clonal cultures drawn from an untreated patient, as well as following *in vitro* drug selection to generate acquired resistance. Suppression of SREBP activity by knocking down both *SREBF1* and *SREBF2* or treatment with fatostatin abrogates this drug resistance phenotype, whereas ectopic *SREBF2* expression alone is sufficient to dramatically enhance vemurafenib resistance.

SREBP2 Induces *TF* Transcription

SREBF1 and *SREBF2* are central players of lipogenesis, with *SREBF1* primarily linked to lipid metabolism and *SREBF2* being the master regulator of cholesterol synthesis. Both SREBP paralogs are known to be aberrantly expressed in some cancers, although their functional significance in carcinogenesis remains poorly understood (32, 33). To determine which *SREBF* genes are functionally important in mediating the melanoma CTC tumorigenic and drug resistance phenotypes, we first compared *SREBF1* and *SREBF2* mRNA expression levels in CTC lines using RNA-seq. All five CTC lines showed higher abundance of *SREBF2* mRNA, compared with *SREBF1* (Supplementary Fig. S4A). Consistent with this finding, higher activity of *SREBF2*, compared with *SREBF1*, is detected by GSVA enrichment scores of *SREBF1/2* target gene expression in these CTC lines (Supplementary Fig. S4B; Supplementary Table S2). We used specific antisense oligos (ASO) to effectively suppress *SREBF1* or *SREBF2* individually, or both together (*SREBF1*-KD, *SREBF2*-KD, and *SREBF1/2*-KD, respectively) in the Mel-167 CTC line (Fig. 3A), quantifying clonogenic growth in soft agar, a well-established correlate of tumorigenesis. *SREBF2*-KD significantly suppresses soft-agar growth, whereas *SREBF1*-KD has no effect (Fig. 3B). The combination of the two ASOs (*SREBF1/2*-KD) demonstrates modestly increased colony suppression, compared with *SREBF2*-KD alone (Fig. 3B, $P = 0.0480$ for *SREBF2*-KD vs. control and $P = 0.0277$ for *SREBF1/2*-KD vs. control). Interestingly, mTOR signaling has been implicated in lipogenic signaling (34), and although its inhibitor Torin 1 suppresses expression of *SREBF1* in Mel-167 CTCs, it does not affect levels of *SREBF2* (Supplementary Fig. S4C and S4D). Thus, although *SREBF1* may enhance the effect of *SREBF2*, the latter is most relevant to Mel-167 CTC tumorigenesis.

To identify *SREBF2*-regulated genes mediating these tumor-enhancing effects, we undertook chromatin immunoprecipitation followed by next-generation sequencing (ChIP-seq), defining direct *SREBF2* transcriptional targets in cultured melanoma CTCs. Well-established SREBP targets implicated in lipogenesis are readily identified by ChIP-seq (Fig. 3C; Supplementary Table S4). However, additional *in vivo* SREBP-binding sites are also identified in the promoters of multiple genes involved in ferroptosis and iron homeostasis (Fig. 3C; Supplementary Table S4), supporting the coordinated expression of these pathways, previously observed in multiple CTC lines (Fig. 1D–F). Key to the intersection between these pathways appears to be the iron-binding protein TF: Comparing the set of genes commonly upregulated across the cultured melanoma CTCs versus primary tumors, metastases, and CCLE melanoma lines ($N = 586$) with the set of genes whose promoters are bound by SREBP2 in CTCs ($N = 3{,}813$), we identified 258 candidate targets, of which the most highly upregulated hit was *TF* (mean fold change = 54.19; Fig. 3D; Supplementary Fig. S5A). In an independent analysis, we compared RNA-seq transcriptional profiles of two melanoma CTC lines versus their individually matched archival tumor specimens: Mel-167 (CTCs vs. matched primary tumor) and PEM-22 (CTCs vs. six patient-matched–independent metastatic lesions). Among 10 differentially expressed transcripts shared in these two pairwise comparisons (genes upregulated > 32-fold in CTCs), *TF* was the most highly differentially expressed (first hit in PEM-22, fourth in Mel-167; Supplementary Fig. S5B). Interestingly, endogenous *TF* expression is also significantly upregulated in the clonally derived Mel-167 CTC lines with intrinsic vemurafenib resistance, compared with the sensitive isogenic clones (Supplementary Fig. S5C). We therefore selected the iron-binding protein TF as a novel candidate SREBP2 target, with potential relevance to lipogenic regulation of iron metabolism and tumorigenesis.

Direct visualization of the ChIP-seq reads confirms a sharp peak of SREBP binding at the site of the *TF* gene promoter (Fig. 3E). The promoter contains two adjacent predicted SREBP-binding sites (Catalog of Inferred Sequence Binding Preferences; ref. 35): motifs M2388_1.02, ATGAGGTGAT, and M6488_1.02, GGGTTGGGAGAGG (Fig. 3F; Supplementary Fig. S5D). Direct *in vivo* binding of SREBP2 to *TF* promoter fragments containing the two predicted sites is evident using ChIP followed by PCR amplification of the DNA sequences (ChIP-qPCR; Fig. 3F; Supplementary Fig. S5D). We note that ASOs targeting *SREBF2* suppress *TF* expression effectively, whereas knockdown of *SREBF1* has a mild effect on *TF* expression in Mel-167 CTCs (Fig. 3G). Soft-agar growth suppression is observed only in *SREBF2*-KD but not in *SREBF1*-KD Mel-167 CTCs (Fig. 3B), and a modest enhancement of *TF* suppression is evident with the combined knockdown (Fig. 3G). mTOR inhibition, which suppresses *SREBF1* but not *SREBF2* expression, also does not affect *TF* expression (Supplementary Fig. S4C and S4D). Finally, to confirm the functional consequence of these chromatin-binding studies, we used doxycycline-inducible *SREBF2*, demonstrating robust induction of *TF* mRNA and TF protein expression in cultured melanoma CTCs (Fig. 3H and I). Taken all together,

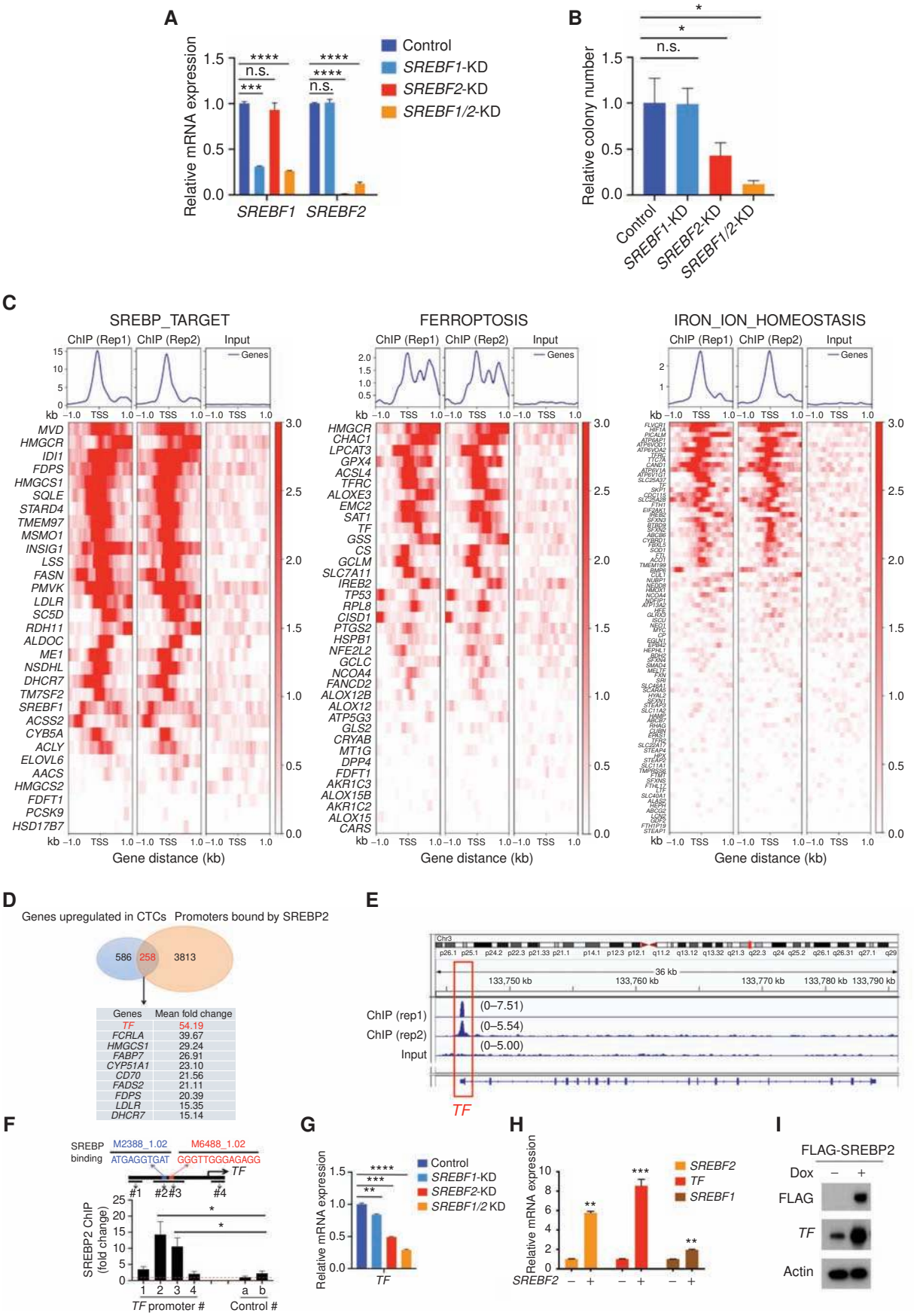

TF is a novel *SREBF2* target gene in melanoma CTCs, raising the possibility that it may contribute to the lipogenic tumorigenesis phenotype through modulation of iron homeostasis and ferroptosis.

TF Enhances Tumorigenesis by Melanoma CTC Cultures

TF plays a critical role in regulating iron trafficking and metabolism. It is normally expressed only in the liver, from which it is secreted into the bloodstream where it binds tightly to iron, ultimately interacting with the TF receptor expressed by multiple cell types and internalized (36). Although expression of the TF receptor (*TFRC*) gene is common in cancer (37), *TF* transcripts are rarely detected except in liver and in some cell types in the brain (38, 39). To exclude the possibility that aberrant *TF* expression in CTCs results from *in vitro* culture conditions, we undertook single-cell RNA-seq of individually picked melanoma CTCs following microfluidic enrichment from primary blood specimens. Among 76 individual CTCs freshly isolated from 22 patients and validated to be melanoma cells by their expression of melanoma lineage markers (24), 7 (9.2%) expressed *TF* mRNA [mean expression = 17.64, transcripts per million (TPM); Fig. 4A]. Such fresh CTCs include both viable and preapoptotic cells with variable RNA quality. However, *TF* expression is detectable in as many as 9 of 20 (45%) single CTCs that have been incubated in culture medium for 4 to 8 weeks, a condition in which only viable CTCs persist, but before they initiate *in vitro* proliferation (mean expression = 90.14 TPM; Fig. 4A). *TF* expression is neither evident in individually selected leukocytes nor detectable in similarly isolated prostate or hormone receptor–positive breast CTCs, suggesting a melanoma-specific pathway (Supplementary Fig. S5E; refs. 25, 40, 41).

Because TF is primarily a secreted protein, we tested whether a fraction might be retained intracellularly. We compared the liver cancer–derived HepG2 cells with the melanoma CTC Mel-167, demonstrating comparable levels of *TF* mRNA (Supplementary Fig. S6A). Minimal baseline levels of TF protein are present in the culture medium that is used to maintain either HepG2 or Mel-167, with or without addition of FBS or B27 supplements (Supplementary Fig. S6B). Following cell culture, TF is detectably secreted into the conditioned medium, and under comparable conditions, we calculate that Mel-167 CTCs secrete 45% of the TF secreted by HepG2 cells (Supplementary Fig. S6C). However, compared with HepG2 cells, Mel-167 CTCs retain 620% higher levels of TF intracellularly (Supplementary Fig. S6D; calculated as 19.22 ng/mL from 1 million cells for Mel-167 vs. 3.10 ng for HepG2 cells), with cell fractionation experiments showing most of the intracellular TF present in cytoplasmic and membrane fractions (Supplementary Fig. S6E). Intracellular retention of TF protein in Mel-167 CTCs may be partially explained by the presence of alternatively spliced transcripts, approximately 1.4% of which lack the secretion signal sequence that spans exons 1 and 2 (Supplementary Fig. S6F and S6G). Alternatively, it is also possible that an increase in secreted TF may result in more recycled TF–TFRC complex within the endosomal compartment.

To determine the functional consequences of aberrant *TF* expression in melanoma CTCs, we tested the effect of two independent short hairpin RNAs (shRNA) in Mel-167 CTCs. *TF* knockdown (*TF*-KD) using either of these shRNA constructs leads to a modest reduction in proliferation under baseline *in vitro* culture conditions (reduced by 34.5% for sh*TF* #1, $P = 0.0272$, and 35.5% for sh*TF* #2, $P = 0.0384$, at day 4 of growth when compared with shControl; Fig. 4B; Supplementary Fig. S7A and S7B), but a marked suppression of clonogenic activity by 65.9% for sh*TF* #1 ($P = 0.0026$) and 84.8% for sh*TF* #2 ($P = 0.0013$) in soft agar (Fig. 4C; Supplementary Fig. S7C). Subcutaneous tumor formation is suppressed by either shRNA construct in Mel-167 CTCs (a reduction in tumor size by 69.2% for sh*TF* #1, $P = 0.0011$, and 88.9% for sh*TF* #2 as compared with shControl, $P = 0.0008$; Fig. 4D), and metastatic colonization following tail-vein injection is abrogated,

Figure 3. *TF* is a transcriptional target of SREBP2. **A,** Knockdown of *SREBF1* (*SREBF1*-KD), *SREBF2* (*SREBF2*-KD), or both (*SREBF1/2*-KD) in Mel-167–cultured CTCs, using ASOs, demonstrating both specificity for each individual gene and effective dual targeting. *y*-axis, relative mRNA fold change normalized to Actin. Statistical significance was assessed by two-sided Welch *t* tests. ***, $P < 0.001$; ***, $P < 0.0001$; n.s, not significant. **B,** Quantification of soft-agar colony numbers formed by Mel-167 CTCs transfected with control, *SREBF1*-KD, *SREBF2*-KD, or *SREBF1/2*-KD ASO sequences. *y*-axis, relative colony number normalized to control. Statistical significance was assessed by two-sided Welch *t* test. *, $P < 0.05$; n.s, not significant. **C,** Heat map representation of SREBP2 ChIP-seq in Mel-167 CTCs, showing enrichment of SREBP2-binding sites within the transcriptional start sites (TSS) of genes comprising three pathways: SREBP_TARGET, FERROPTOSIS, and IRON_ION_HOMEOSTASIS. For each pathway, the first two columns represent replicate experiments, and the third shows the input reads. The GSEA pathway enrichment plots and assessment of statistical significance of SREBP2 ChIP-seq are shown in Supplementary Table S4. The heat map color scale (*y* axis) represents the read intensities in bins per million mapped reads (BPM: set the maximum value at 3). **D,** Venn diagram showing the top 10 genes at the intersection of SREBP2-bound promoters in CTCs and genes with increased expression in CTCs, compared with primary and metastatic melanoma (TCGA) and standard tumor-derived melanoma lines (CCLE). The mean fold change in individual gene expression is listed below the Venn diagram, with *TF* as the top hit. **E,** Integrative Genomic Viewer (IGV) plot showing SREBP2 ChIP-seq peaks in the *TF* gene promoter region (framed in red). Two experimental repeats (rep 1 and rep 2) are shown. Input genomic DNA serves as control. The scales in BPM of peak window for each sample are shown in brackets, and the genomic structure of the *TF* gene is shown below the IGV plot. **F,** *In vivo* binding of SREBP2 to the *TF* gene promoter, as shown by ChIP-qPCR analysis in Mel-167 melanoma CTCs. Top, schematic representation of expected qPCR products (#1, 2, 3, 4) spanning regions of the *TF* gene promoter including those containing the two predicted SREBP-binding sites (#2, 3), which are shown in blue and red (35). Bottom, ChIP-qPCR performed using anti-FLAG antibody to precipitate FLAG–SREBP2–DNA complexes. *y*-axis shows relative fold enrichment of *TF* gene promoter fragments (normalized to control IgG antibody), with strong *in vivo* binding of SREBP2 to fragments #2 and #3 that contain the SREBP consensus sequences, but not to neighboring fragments (#1 and #4) or to unrelated sequences (a, b). Data are normalized to 2% of total genomic DNA input. **G,** Suppression of *TF* mRNA expression in Mel-167 CTCs, following treatment with ASOs targeting *SREBF1* and *SREBF2* alone or together, compared with control (see **A** for knockdown efficiency and specificity), demonstrating that SREBP2 is the primary regulator of *TF* expression, with modest enhancement by combined *SREBF1/2*-KD. Statistical significance was assessed by two-sided Welch *t* tests. **, $P < 0.01$; ***, $P < 0.001$; ****, $P < 0.0001$. **H,** Induction of *TF* mRNA expression by SREBP2 in Mel-167 CTCs, demonstrated by qRT-PCR analysis, 48 hours following doxycycline-mediated inducible expression of *SREBF2*. *SREBF2* also mediates a modest increase in *SREBF1* mRNA. Data are normalized to actin. *y*-axis shows relative fold change in *SREBF2*-expressing cells compared with uninduced controls. Statistical significance was assessed by two-sided Welch *t* test. $P = 0.003$ for *TF*; $P = 0.0002$ for *SREBF2*; $P = 0.0009$ for *SREBF1* (**, $P < 0.01$; ***, $P < 0.001$). **I,** Induction of *TF* protein by doxycycline-inducible FLAG-tagged *SREBF2*, quantified by Western blot analysis in Mel-167 CTCs. Actin is shown as loading control.

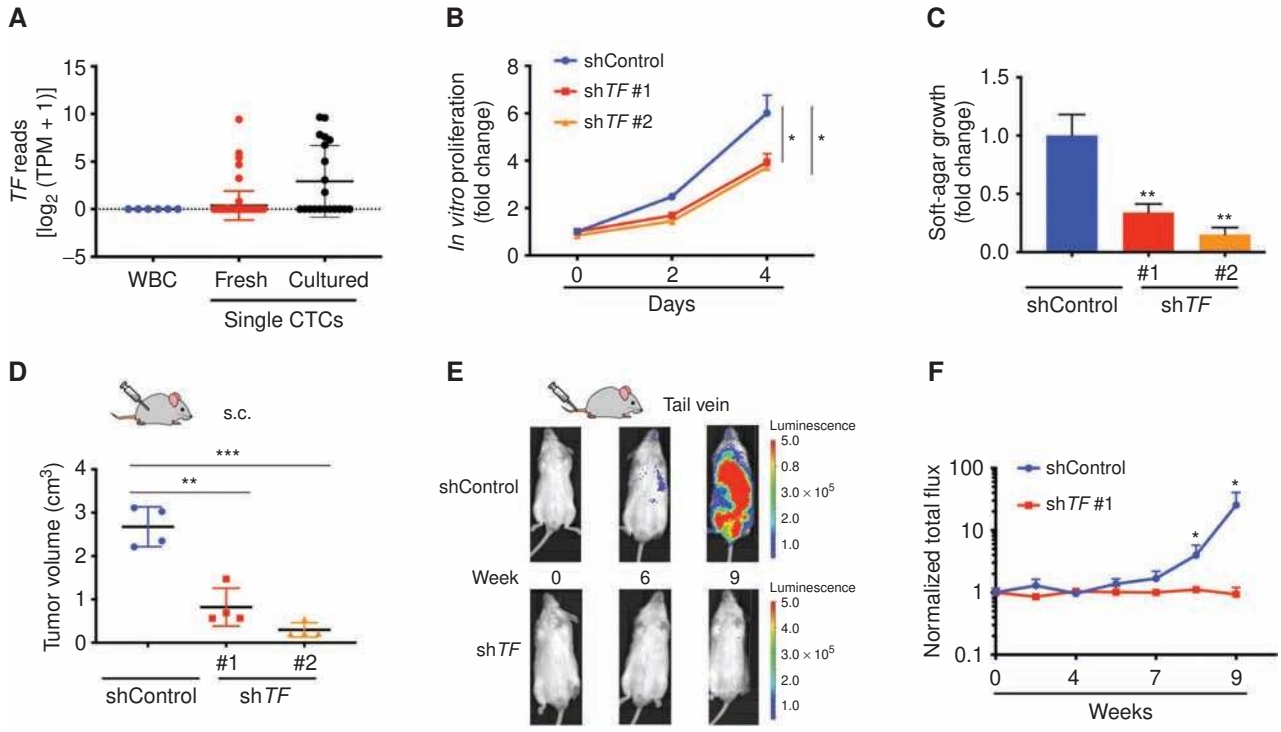

Figure 4. Depletion of *TF* impairs tumor formation. **A,** Expression of *TF* transcripts within single melanoma CTCs freshly isolated from patients with metastatic melanoma by microfluidic negative depletion platform ($n = 76$ single CTCs from 22 patients), or in CTCs that were incubated in culture medium for <8 weeks after microfluidic isolation. Short-term culture ensures collection of viable CTCs with intact RNA and precedes the initiation of *in vitro* proliferation ($n = 20$ single CTCs). The fresh and cultured single CTCs are compared with contaminating leukocytes (WBC), from healthy donor blood identically processed through the microfluidic chip (WBC; $n = 6$). *Y* axis, $\log_2$ (TPM+1). **B,** Modest suppression of *in vitro* proliferation by Mel-167 CTCs, following *TF*-KD mediated by either of two independent shRNA constructs (knockdown efficacy shown in Supplementary Fig. S7A) compared with cells transfected with shControl. Two-sided Welch *t* test was employed to assess the differences in proliferation rates between sh*TF* and shControl at day 4. *y*-axis, relative fold change normalized to day 0. *, $P < 0.05$. **C,** Reduction in soft-agar colony formation by Mel-167 melanoma CTCs, following *TF*-KD using two independent shRNA constructs, versus shControl (see Supplementary Fig. S7A). Colonies were quantified by automated imaging at 4 weeks. Statistical significance from four independent experiments was assessed by two-sided Welch *t* test. **, $P < 0.01$. *y*-axis, relative fold change normalized to shControl. **D,** Suppression of subcutaneous melanoma formation by Mel-167 CTCs, following *TF*-KD. Tumor volume following subcutaneous inoculation of tumor cells was quantified using 4 mice per experimental condition. Statistical significance was assessed by two-sided Welch *t* test. **, $P < 0.01$; ***, $P < 0.001$. **E** and **F,** Abrogation of intravenous (tail-vein) metastasis by Mel-167 melanoma CTCs following *TF*-KD. **E,** Metastatic burden was monitored in GFP-luciferase–tagged CTCs using live imaging (IVIS), with representative images shown at time points 0, 6, and 9 weeks after injection. CTCs were infected prior to injection with either sh*TF* or scrambled shRNA controls. **F,** Time-course showing the quantification of metastatic tumors by *in vivo* luciferase imaging. *y*-axis, averaged total flux of luciferase signal; sh*TF* ($n = 4$) and shControl ($n = 4$) mice. Statistical significance was assessed by two-sided Welch *t* test: $P = 0.047$ for week 8 comparisons and $P = 0.046$ for week 9 comparisons. *, $P < 0.05$. Tissue-specific histologic quantitation of metastases (lungs, liver, and kidneys) is shown in Supplementary Fig. S7D–S7F.

as measured by whole-mouse imaging [*in vivo* imaging system (IVIS); Fig. 4E and F], as well as histologic analysis of lung, liver, and kidney metastases (Supplementary Fig. S7D–S7F).

To confirm the specificity of this effect, we generated a synthetic *TF* cDNA, in which mutation of three third-position nucleotides in the coding region of *TF* confers resistance to knockdown by sh*TF* #1, without affecting expression levels (TF^{ALT}, Supplementary Fig. S8A and S8B). In Mel-167, as well as in Mel-182-2, a second, independently isolated CTC line derived from another patient with metastatic melanoma, *TF*-KD was effectively rescued by ectopic expression of TF^{ALT}, resulting in restitution of *TF* mRNA and protein expression (Supplementary Fig. S8C–S8F). In both CTC-derived cell lines, *TF* depletion leads to the suppression in soft-agar colony growth, which is largely rescued by overexpression of TF^{ALT} (Mel-167: $P = 0.0004$ comparing sh*TF* #1 with sh*TF* #1 + Rescue; Mel-182-2: $P = 0.0027$ comparing sh*TF* #1 with Control; $P = 0.0159$ comparing sh*TF* #1 with sh*TF* #1 + Rescue; Supplementary Fig. S8G and S8H). Therefore, in melanoma CTCs that have acquired aberrant expression of *TF*, its suppression compromises tumorigenic phenotypes.

TF Modulates Ferroptotic Cell Death

Although the function of TF in regulating iron levels in the blood circulation is well established, it may also play a role in regulating intracellular iron through a sequestration mechanism, similar to iron-complexed ferritin, the primary source of intracellular iron storage (42). Depletion of intracellular iron may compromise key iron-dependent pathways, whereas its overabundance may trigger iron-dependent cell death pathways, such as ferroptosis (43, 44). Gene set enrichment analysis (GSEA) shows a predominant signaling pathway upregulated in *TF*-KD Mel-167 CTCs to be "REACTIVE_OXYGEN_SPECIES" ($P = 0.0049$, Fig. 5A; Supplementary Table S5). Indeed, *TF*-KD cells have a significant increase in ROS compared with shRNA controls, as measured

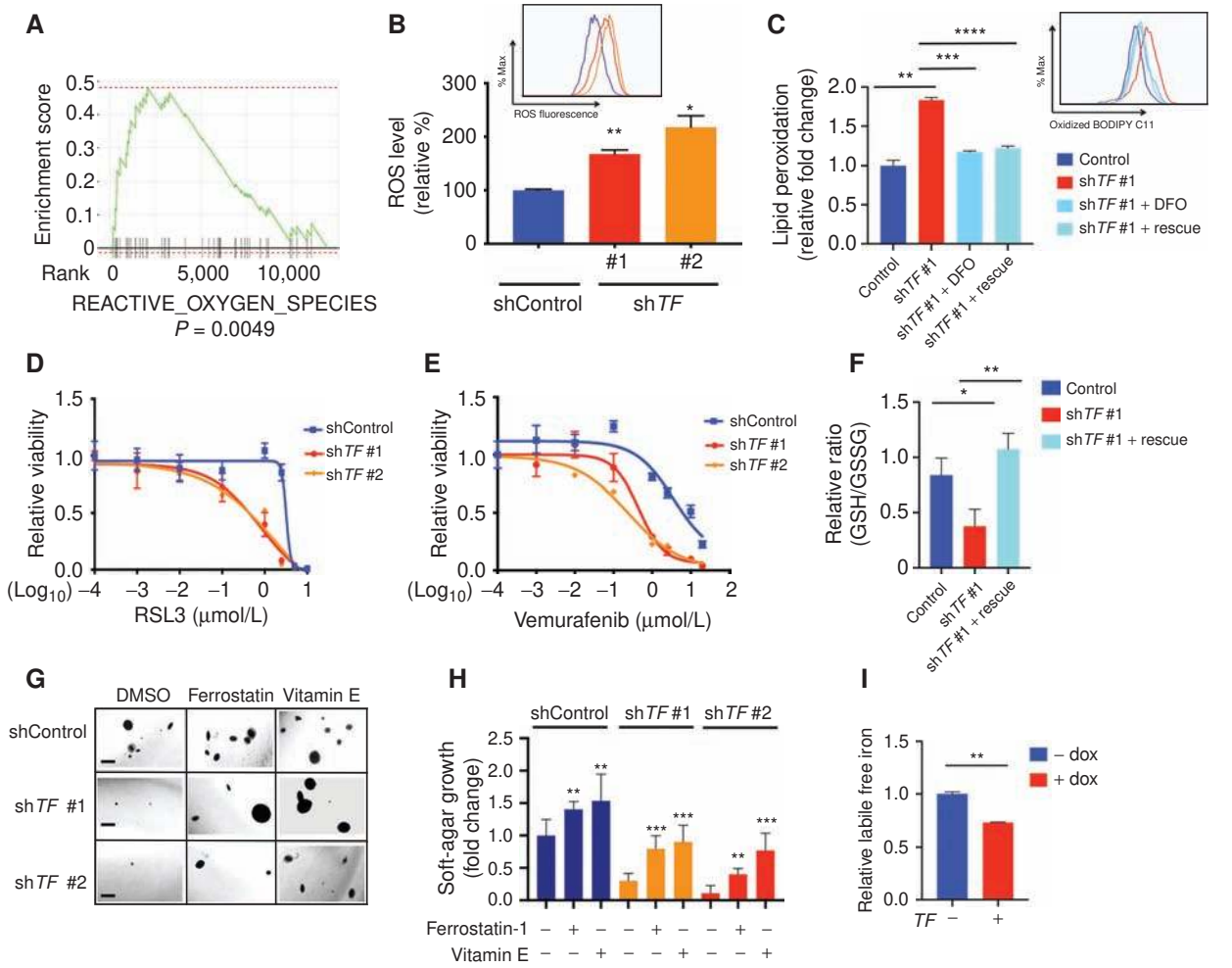

Figure 5. *TF* modulates ferroptotic cell death. **A,** GSEA pathway enrichment plot showing significant downregulation of "REACTIVE_OXYGEN_SPECIES" pathway following *TF*-KD in Mel-167 melanoma CTCs, compared with shControl. **B,** Increased intracellular ROS in Mel-167 melanoma CTCs following *TF*-KD, using two independent shRNA constructs (#1, #2), compared with scrambled construct (shControl). ROS was quantified by flow cytometric analysis with a fluorescent ROS probe, and the geometric mean of fluorescence signal was calculated for each group. The differences between the two groups were assessed by two-sided Welch *t* test. Statistical significance: $P = 0.0028$ for sh*TF* #1 compared with shControl; $P = 0.0104$ for sh*TF* #2 compared with shControl. *, $P < 0.05$; **, $P < 0.01$. **C,** Quantification of lipid peroxidation levels by flow cytometry in Mel-167 CTCs following knockdown of *TF* (sh*TF* #1), compared with shControl cells. The increase in lipid peroxidation induced by *TF*-KD is abolished either by the addition of the iron chelator DFO (50 μmol/L with preincubation for 12 hours before flow cytometric assay) or by expression of TF^{ALT} cDNA (rescue), a synthetic construct in which mutation of three third-position noncoding nucleotides renders *TF* resistant to targeting by sh*TF* #1 without affecting expression levels (see Supplementary Fig. S8A and S8B). Lipid peroxidation is measured using BODIPY 581/591 C11 molecular sensor, the fraction of cells positive for lipid peroxidation was calculated, and data were normalized to shControl. *y*-axis, fold change. Statistical significance was assessed by two-sided Welch *t* test. **, $P < 0.01$; ***, $P < 0.001$; ****, $P < 0.0001$. **D,** *TF*-KD enhances Mel-167 melanoma CTC cytotoxicity by the ferroptosis inducer RSL3. *TF*-KD was achieved using two different shRNAs and compared with scrambled shControl. *y*-axis, relative cell viability. *x*-axis, drug concentrations (μmol/L) in $\log_{10}$ scale. Statistical significance was assessed by two-sided Welch *t* test. When sh*TF* #1 is compared with shControl: 1 μmol/L, $P = 0.0001$; 2.5 μmol/L, $P = 0020$. When sh*TF* #2 is compared with shControl: 1 μmol/L, $P = 7.69 \times 10^{-5}$; 2.5 μmol/L, $P = 0021$; 5 μmol/L, $P = 0179$. **E,** *TF*-KD increases sensitivity to vemurafenib in $BRAF^{V600E}$-mutant melanoma Mel-167 CTCs. *TF*-KD was achieved using two different shRNAs and compared with scrambled shControl. *y*-axis, relative cell viability. *x*-axis, drug concentrations (μmol/L) in $\log_{10}$ scale. Statistical significance was assessed by two-sided Welch *t* test. When sh*TF* #1 is compared with shControl at different drug concentrations: 0.1 μmol/L, $P = 0.0246$; 1 μmol/L, $P = 2.07 \times 10^{-5}$; 2.5 μmol/L, $P = 2.14 \times 10^{-6}$; 10 μmol/L, $P = 0.0001$; 20 μmol/L, $P = 0.0007$. When sh*TF* #2 is compared with shControl: 0.01 μmol/L, $P = 0.0010$; 0.1 μmol/L, $P = 0.0004$; 1 μmol/L, $P = 9.38 \times 10^{-6}$; 2.5 μmol/L, $P = 8.70 \times 10^{-5}$; 10 μmol/L, $P = 0.0006$; 20 μmol/L, $P = 0.0011$. **F,** Reduced ratio of GSH/GSSG in *TF*-KD Mel-167, compared with vector control. A synthetic TF^{ALT} cDNA, resistant to sh*TF* #1 knockdown, rescues the phenotype (see Supplementary Fig. S8A and S8B). *y*-axis, relative ratio between GSH and GSSG levels. Data are calculated based on three independent biological repeats, and statistical significance was assessed by two-sided Welch *t* test. $P = 0.0216$, comparing sh*TF* #1 with control and $P = 0.0047$ comparing sh*TF* #1 + Rescue with sh*TF* #1. *, $P < 0.05$; **, $P < 0.01$. **G,** Suppression of soft-agar colony formation by Mel-167 CTCs following *TF*-KD by two different shRNAs (scrambled shRNA control). The clonogenic phenotype is rescued by two lipophilic antioxidants, ferrostatin-1 (0.5 μmol/L) and vitamin E (20 μmol/L). Representative images for each condition are shown. Scale bar, 500 μmol/L. **H,** Quantitation of colony formation in soft agar shown in **F**. Differences between the two groups were assessed by two-sided Welch *t* test. Statistical significance: **, $P < 0.01$; ***, $P < 0.001$. **I,** Quantitation of intracellular labile free iron in Mel-167 CTCs, using flow cytometry measurements of a fluorescent reporter (Goryo Chemical, Inc.). The normalized geometric mean of fluorescence intensity was calculated in CTCs expressing doxycycline (dox)-inducible *TF* after 48 hours of doxycycline treatment. Statistical significance was assessed by two-sided Welch *t* test (**, $P < 0.01$). Similar results using Mel182-2 CTCs are shown in Supplementary Fig. S8N.

by a fluorescent reporter (68% increase for sh*TF* #1, $P = 0.0028$; 118% increase for sh*TF* #2, $P = 0.0104$; Fig. 5B). Similarly, lipid peroxidation is strikingly increased in *TF*-KD melanoma CTCs, compared with controls (Fig. 5C). This effect is iron-dependent because cotreatment of Mel-167 CTCs with the iron chelator deferoxamine (DFO; 50 μmol/L) results in restoration of lipid ROS to normal levels, comparable to those observed following *TF* rescue through expression in Mel-167 CTCs of the synthetic shRNA-resistant cDNA TF^{ALT} (Fig. 5C). Similar effects on lipid peroxidation following *TF*-KD and rescue by either DFO or the TF^{ALT} construct are evident in the second CTC line Mel-182-2 (Supplementary Fig. S8I).

Consistent with these findings, *TF*-KD CTCs show increased sensitivity to the ferroptosis inducer RSL3 (45) compared with control, indicating that the increased ROS and lipid peroxidation are correlated with heightened susceptibility to ferroptosis (Fig. 5D). Mel-167 CTCs, which carry the $BRAF^{V600E}$ mutation, also show increased sensitivity to vemurafenib following *TF*-KD (Fig. 5E), suggesting that failure to suppress lipid peroxidation may also result in enhanced killing by BRAF inhibitors in melanoma CTCs. Previous studies have reported that BRAF inhibitor–resistant melanoma cells exhibit increased sensitivity to ferroptosis (46, 47), suggesting cross-talk between these two druggable survival pathways. Ferroptosis itself is dependent on GPX4, which detoxifies lipid ROS at the expense of reduced GSH, leading us to assess the GSH/GSSH ratio as a measure of redox balance. Indeed, the ratio of GSH/GSSG is significantly reduced in sh*TF*-treated cells, an effect that is rescued by expression of the synthetic TF^{ALT} construct (Fig. 5F; total GSH and GSSG levels are shown in Supplementary Fig. S8J and S8K). Given the potent effect of *TF*-KD on soft-agar clonogenic potential of melanoma CTCs, we tested a number of experimental rescue conditions. Both the antiferroptosis drug ferrostatin-1 (0.5 μmol/L) and the lipophilic antioxidant vitamin E (50 μmol/L) partially rescued the clonogenic suppression mediated by either of the two *TF* shRNA constructs (Fig. 5G and H). Both of these antioxidants also have a moderate effect on baseline soft-agar colony formation by melanoma CTCs. These observations are consistent with the role of TF expression in quenching intracellular free iron within melanoma CTCs.

To test the potential TF iron sequestration mechanism, we generated Mel-167 and Mel-182-2 CTCs with ectopic overexpression of *TF*. In both CTC lines, TF overexpression (Supplementary Fig. S8L and S8M) results in a significantly reduced pool of labile free iron, consistent with a sequestration mechanism (Fig. 5I; Supplementary Fig. S8N). To further test the functional effects of *TF* overexpression, we selected the CCLE melanoma cell line IGR-37, which does not express high levels of endogenous *TF*. Ectopic overexpression of *TF* in these cells leads to a reduction in lipid peroxidation (Supplementary Fig. S9A and S9B). Interestingly, ectopic expression of the mature and activated *SREBF2* similarly reduces lipid peroxidation (Supplementary Fig. S9A and S9B). Ectopic overexpression of either *TF* or *SREBF2* in IGR-37 melanoma cells also confers relative resistance to the ferroptosis inducer RSL3 (Supplementary Fig. S9C and S9D). Altogether, these observations support a model whereby *TF* expression regulates the intracellular labile free iron pool, affecting ROS and lipid peroxidation, with consequences for cellular susceptibility to ferroptosis.

The concordant expression of lipogenic and iron metabolic pathways observed in melanoma CTCs raises the possibility that these two pathways are mutually interregulated. We have shown that SREBP2 binds to the *TF* gene promoter and directly induces its expression, but modulation of TF levels themselves appears to affect SREBP targets, potentially through more indirect mechanisms. Indeed, *TF*-KD in melanoma CTCs leads to a reduction in expression of SREBP target genes: GSEA pathway analysis of RNA-seq data in *TF*-KD CTCs identifies lipogenesis as the most prominently downregulated pathway category, such as "SREBP_TARGET" ($P = 0.0024$, as well as "SREBF1/2_TARGET," $P = 0.0022$ for both pathways) and "CHOLESTEROL_HOMEOSTASIS" ($P = 0.0025$; Fig. 6A and B; Supplementary Table S5). Conversely, ectopic expression of *TF* leads to upregulation of the downstream SREBP target transcripts *SCD* and *ACSL1* (Fig. 6C; Supplementary Fig. S8M). Furthermore, the suppression of ACSL1 protein expression resulting from shRNA knockdown of *TF* is fully rescued by expression of the non-degradable TF^{ALT} construct (Supplementary Fig. S8E and S8F). Interestingly, addition of cholesterol (10 μg/mL), an endpoint of lipogenic pathways, rescues *TF*-KD clonogenic suppression (Fig. 6D and E). Thus, the iron homeostasis and lipogenic pathways appear to be mutually coregulated in melanoma CTCs, with SREBP2 directly activating the *TF* promoter, whereas TF expression may lead more indirectly to modulation of SREBP target gene expression and lipogenesis.

Coregulation of SREBP and Iron Transport Pathways in Patient-Derived Primary CTCs

To extend these findings from cultured melanoma CTCs to freshly isolated individual CTCs from patients with metastatic melanoma, we undertook comprehensive single-cell RNA-seq of 76 individual CTCs collected from 22 patients using microfluidic CTC-iChip isolation, followed by confirmation of cell identity by expression of melanoma lineage markers (Fig. 7A). Hierarchical clustering analysis reveals a well-demarcated subpopulation of CTCs, "cluster 2," comprising 43 of the 76 single CTCs (57%), with concerted upregulation of lipogenic programs ("SREBF2_TARGET," "ADIPOGENESIS," and "FATTY_ACID_METABOLISM"), iron homeostasis signatures ("IRON_ION_HOMEOSTASIS"), and proliferation ("MYC_TARGETS_V1 & V2"; comparing Cluster 2 vs. Cluster 1 CTCs, Fig. 7A; Supplementary Fig. S10A–S10D; Supplementary Table S6). Cluster 2 CTCs also show signatures of increased energy production that is iron-dependent ("OXIDATIVE_PHOSPHORYLATION"; Fig. 7A; Supplementary Table S6). The enrichment of these pathways in Cluster 2 CTCs remains significant even if only CTCs from patients receiving immunotherapy were analyzed (a total of 53 CTCs from 18 patients; Supplementary Table S6). Because the majority of patients with melanoma whose CTCs were analyzed here were enrolled on immune checkpoint therapies and some were treated with BRAF/MEK-targeted therapies (Supplementary Table S7), hence we were able to test whether these signatures were associated with responsive disease (RD) or progressive disease (PD), as measured by clinical imaging within a median of 74 days (-4 to 122) after CTC sampling

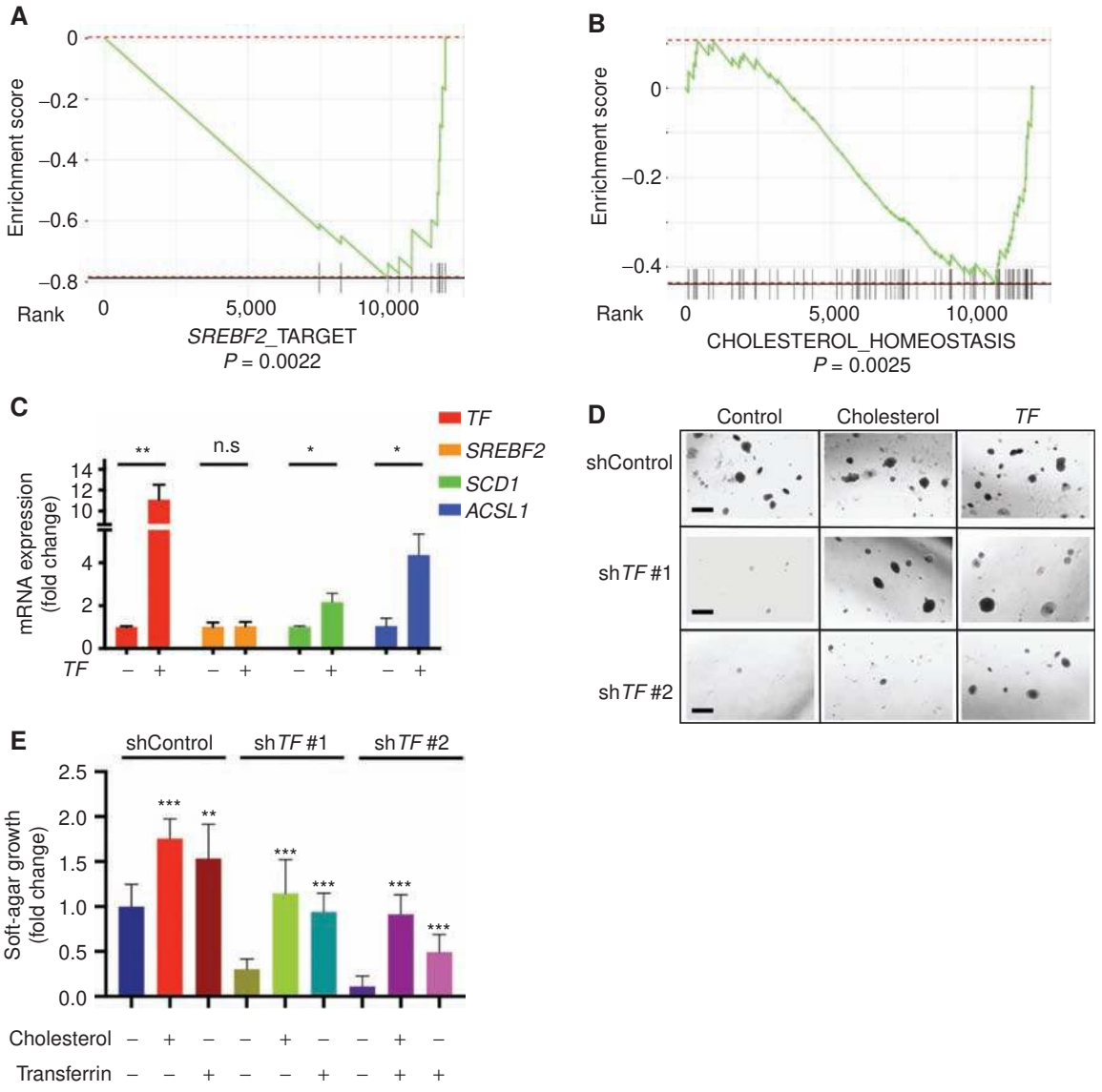

Figure 6. *TF* expression modulates SREBP2 targets. **A** and **B,** Suppression of lipogenic pathways following *TF*-KD in Mel-167 melanoma CTCs. GSEA pathway enrichment plot showing significant downregulation of (**A**) "SREBP_2_TARGET" and (**B**) "CHOLESTEROL_HOMEOSTASIS", in *TF*-KD CTCs, compared with shControl. **C,** Induction of downstream lipogenic effectors, following doxycycline (dox)-inducible expression of *TF* in Mel-167 CTCs (*TF* was induced within 96 hours after virus infection). Expression of *SREBF2* mRNA and its downstream targets genes *SCD* and *ACSL1* are shown (qRT-PCR). Cells were grown under reduced nutrient conditions (RMPI with 2% B27) to sensitize SREBP2 activity. *y*-axis, relative fold change in *TF*-overexpressing CTCs compared with control without dox treatment. Actin was used for internal normalization. Data were obtained from three independent biological repeats. Statistical significance was assessed by two-sided Welch *t* test. $P = 0.007$ for *TF*; $P = 0.868$ for *SREBF2*; $P = 0.039$ for *SCD*; $P = 0.017$ for *ACSL1*. *, $P < 0.05$; **, $P < 0.01$; n.s, not significant. **D** and **E,** Rescue by exogenous cholesterol of soft-agar colony formation defect in Me-167 melanoma CTCs following *TF*-KD with two different shRNAs. Scrambled shRNA was used as control (shControl). Cultures were incubated with either 10 μg/mL cholesterol or 10 μg/mL recombinant *TF* protein (control). Representative images are shown in **D** (scale bar, 500 μm), and quantification of colonies is shown in **E**. The differences between two groups were assessed by two-sided Welch *t* test. Statistical significance: **, $P < 0.001$; ***, $P < 0.0001$.

(disease response was defined using RECIST1.1; see Supplementary Table S7). Within a given patient blood draw containing two or more CTCs, a high (>60%) fraction of CTCs expressing signatures of "Lipogenesis" (SREBF2_TARGET), "Proliferation" (MYC_TARGETS_V2), and "Iron_Homeostasis" (IRON_ION_HOMEOSTASIS; GSVA row Z-score > 0) was highly associated with treatment failure, irrespective of treatment modality (Fig. 7B). Breaking these down into individual gene expression signatures, for patients with a high "Lipogenesis" signature, 5 of 6 progressed on therapy, versus 0 of 10 patients with low-signature CTCs ($P = 0.0014$); for patients with high "Proliferation" CTCs, 4 of 5 progressed on treatment, compared with 1 of 11 patients with low-signature CTCs ($P = 0.0128$); for patients with a high "Iron_Homeostasis" signature, 4 of 6 progressed, compared with 1 of 10 patients with low-signature CTCs ($P = 0.0357$); finally, for patients with a high "Oxi_Phos" signature, 3 of 4 progressed, compared with 2 of 12 patients with a low signature

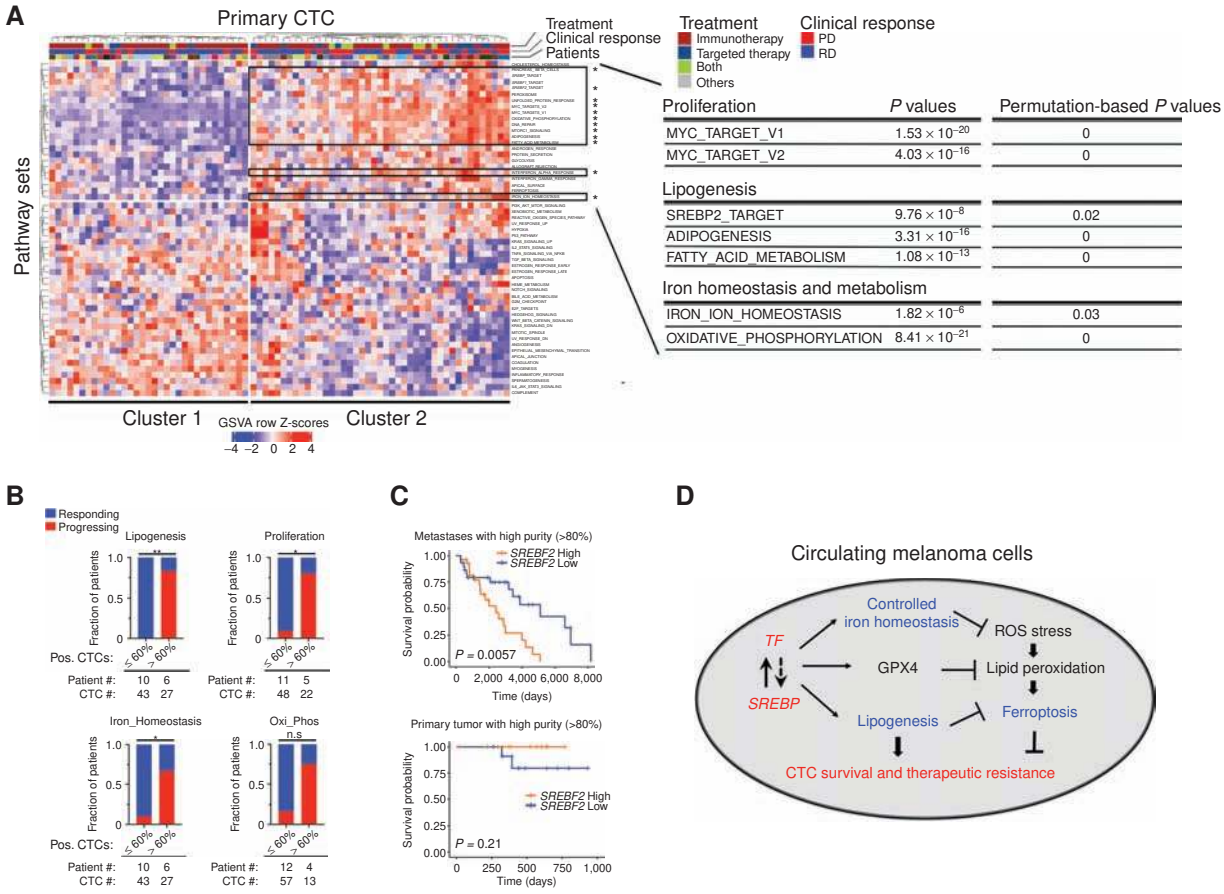

Figure 7. Coordinated upregulation of lipogenesis and iron homeostasis gene expression in patient-derived melanoma CTCs is correlated with poor clinical outcome. **A,** Heat map showing hierarchical clustering (Euclidean distance with complete linkage) of GSVA enrichment scores of pathways across 76 primary single CTCs obtained from 22 patients with metastatic melanoma (CTC lineage confirmed by expression of at least one melanoma-specific marker; ref. 24; see Supplementary Fig. S10 for CTC validation). The first row indicates treatment information of patients, from whom CTCs were isolated, that receive Immunotherapy (colored in dark red), Targeted therapy (dark blue), Both (Immunotherapy + Targeted therapy), or Others (gray). The second row indicates responding (blue) versus progressing (red) patients, and the third row indicates individual patients with color codes. The top right block framed in black shows the subset of CTC samples (Cluster 2) with significantly enriched pathways marked by asterisks. Selected pathways upregulated in Cluster 2 CTC group versus Cluster 1 CTC group are listed on the right (mean difference in GSVA enrichment scores between C1 and C2 > 0.20, FDR-adjusted *P* value < 0.05). Permutation-based *P* values were calculated as "the number of background *P* values lower than the observed *P* values from **A**" divided by "the number of permutations which is 1,000," as shown on the top right. GSVA scores of each pathway and expression levels of all genes within each selected pathway were listed in Supplementary Table S6. **B,** Stacked bar graphs showing the fraction of patients with either RD (blue) or PD (red), whose CTC populations were stratified by low (≤60%) or high (>60%) percentages of CTCs expressing markers of "Lipogenesis (SREBP_2_TARGET)" (top left), "Proliferation (MYC_TARGETS_V2)" (top right), "Iron_Homeostasis (Iron_Ion_Homeostasis)" (bottom left), and "Oxi_Phos (OXIDATIVE_PHOSPHORYLATION)"(bottom right), using GSVA row Z-score > 0 as a cutoff for each pathway signature. Only samples with two or more CTCs were included. The Fisher exact test was performed to assess the association between CTC pathway signature expression and clinical outcome (*, $P < 0.05$; **, $P < 0.01$; n.s, not significant). Clinical assessment of response or progression was ascertained after either immunotherapies or targeted therapies with a median time of 74 days following CTC collection. **C,** Kaplan–Meier plots of disease-specific survival in patients with either metastatic (top) or primary (bottom) melanoma, classified according to *SREBF2* mRNA expression. TCGA Skin Cutaneous Melanoma (SKCM) high-purity melanoma samples (>80% tumor composition) were divided into "*SREBF2* high" (*SREBF2* mRNA expression higher than 75th percentile, orange) and "*SREBF2* low" (*SREBF2* mRNA expression lower than 25th percentile, blue) groups. Kaplan–Meier curves were plotted for disease-specific survival, and *P* values were calculated using the log-rank test. *y*-axis, disease-specific survival probability; *x*-axis, time in days. **D,** Schematic model for coordinated expression of lipogenic and iron homeostatic pathways. The master lipogenic regulator *SREBF2* directly induces expression of the iron carrier *TF*, whereas TF-mediated activation of *SREBP* signaling appears to be indirect. Increased intracellular *TF* reduces iron levels, ROS stress, and lipid peroxidation, all of which serve to suppress ferroptosis and enhance CTC survival and drug resistance. Increased lipogenesis mediated by *SREBP*, including expression of the *SREBF2* target GPX4 (Fig. 3C), similarly reduces ferroptosis. This coordinated cross-talk mechanism between lipogenic and iron homeostatic pathways contributes to CTC-mediated tumorigenesis and therapeutic resistance.

($P = 0.0632$; Fig. 7B). Thus, sampling CTC transcriptomic heterogeneity by single-cell pathway-level analyses within a patient blood sample may identify subclonal populations of CTCs, with treatment-resistant signatures, correlated with adverse clinical outcome. Extending from these small pilot studies to large clinical datasets, we find that *SREBF2* expression itself is highly correlated with reduced survival in patients with metastatic melanoma (TCGA high-purity metastases samples, $P = 0.0057$), irrespective of treatment modality, an association that is not observed in localized primary tumors (TCGA high-purity primary tumor, $P = 0.21$; Fig. 7C; Supplementary Fig. S10E; Supplementary Table S8).

DISCUSSION

Cancer heterogeneity is increasingly recognized as a major cause of therapeutic resistance, with outgrowth of either preexisting or treatment-induced clonal subpopulations ultimately leading to disease progression (48). CTCs, comprising single metastatic precursor cells circulating in the bloodstream, thus provide an exceptional window into the diversity of drug-resistant phenotypes, while at the same time offering insight into vulnerabilities of cancer cells as they briefly transit through the high-oxygen blood environment (49). In this study using single-cell RNA-seq applied to melanoma CTCs, we have uncovered the aberrant coexpression of the lipogenic regulator SREBP2 and the iron-binding protein TF, modulating the cellular response to ferroptosis, with implications for both tumorigenesis and drug resistance (Fig. 7D). In both melanoma CTC-derived long-term cultures and individual CTCs freshly isolated from patient-derived blood specimens, we find coregulation of lipogenic and iron homeostasis pathways. Together, they denote a subset of CTCs with treatment-resistant phenotypes, associated with an adverse clinical outcome. Before initiation of BRAF-targeted therapy, we established multiple clonally derived CTC lines from a single patient with melanoma, demonstrating a degree of cellular heterogeneity in intrinsic drug susceptibility that is correlated with endogenous SREBP activity. As these cultured CTCs are treated with vemurafenib, they display further overexpression of endogenous SREBP, and direct ectopic manipulation of *SREBF2* profoundly modulates their drug sensitivity.

SREBPs are aberrantly activated in several cancer types, including subsets of glioblastoma, melanoma, kidney cancer, prostate cancer, and breast cancer (32, 50–53). Although previous studies have linked PI3K and KRAS oncogenic signals to SREBP1/2 activation (34, 51, 54), the actual consequences of SREBP1/2 signaling on tumorigenesis are uncertain. SREBP2 ChIP-seq studies identify core target genes involved in cholesterol synthesis, glucose breakdown, and fatty acid synthesis, which may contribute to supporting the increased bioenergetic demands of proliferating tumor cells (33, 55). In the context of melanoma CTCs, however, we unexpectedly observed that a substantial fraction of SREBP2-bound promoters regulate genes involved in iron homeostasis, in addition to classic lipogenic genes. Among these, *TF* is noteworthy for both its level of induction by SREBP2 and the dramatic consequences of its knockdown on tumorigenesis and metastasis phenotypes.

The intracellular functions of the iron-binding transporter TF are poorly characterized. In CTCs with elevated endogenous *TF* expression, we find that its knockdown increases intracellular ROS and lipid peroxidation, lowering the GSH/GSSG ratio and mediating a reduction in soft-agar colony formation that is rescued by the lipophilic antioxidants ferrostatin and vitamin E. *TF*-KD also enhances cellular sensitivity to the ferroptosis inducer RSL3, as well as to the BRAF inhibitor vemurafenib. Conversely, overexpression of *TF* in CTCs reduces labile free iron pools, consistent with a sequestration mechanism, and its ectopic expression in melanoma cells that lack endogenous *TF* expression leads to reduced lipid peroxidation and increased resistance to RSL3. Although most *TF* protein is secreted from cells, a fraction is retained intracellularly, likely the result of alternative pre-mRNA splicing that excludes the 5′ secretion signal sequence. Although we favor the concept that TF mediates iron sequestration intracellularly, we cannot exclude the possibility that it binds iron within the extracellular microenvironment, thereby reducing intracellular iron levels. As such, an iron-transporting protein that is physiologically secreted by liver cells into the bloodstream appears to have been adapted by some cancer cells to help regulate intracellular iron levels.

The essential role of iron in heme biosynthesis and in multiple enzymatic reactions is well established, but the contribution of cellular iron levels to spontaneous and drug-induced ferroptosis is increasingly appreciated as a critical feature of cancer cell biology that may be harnessed to modulate existing therapies (43, 44, 56). TF is physiologically produced by the liver, and it regulates iron homeostasis through the *TFRC*, which is expressed in most tissues. Although *TFRC* is overexpressed in many tumors (37, 57), TF itself has not been implicated in malignancy. In *TFRC*-overexpressing cells, addition of iron-loaded TF to the culture medium increases iron import and appears to promote ferroptosis through iron overload (58). In contrast, in the setting of melanoma CTCs with endogenous expression of TF, it appears to function as a quencher of intracellular iron, leading to suppression of ferroptosis. Consistent with the importance of tightly regulated intracellular iron pools, we find that intracellular TF protein is abundant in melanoma CTCs, and its suppression increases their levels of ROS and oxidized lipids. Thus, melanoma CTCs appear to have hijacked this liver-specific gene to modulate the availability of labile iron pools, oxidative stress, and ferroptosis sensitivity.

The functional consequences of TF overexpression in melanoma CTCs appear to be considerable. Suppression of endogenous *TF* in these cells dramatically abrogates their blood-borne metastatic potential and to a lesser extent their primary tumorigenesis. Soft-agar clonogenic ability is also suppressed by *TF*-KD, with a relatively modest effect on *in vitro* proliferation. Together, these observations highlight the important role played by ROS stress in controlling metastatic propensity, and they point to the unexpected role of a major iron-transporting protein in mediating resistance to oxidative stress. The role of oxidative stress in the blood circulation as a critical suppressor of cancer metastasis has recently emerged, through the paradoxical role of antioxidants as prometastatic effectors (17, 59–62). Indeed, although early studies had pointed to the cellular damage and potential tumorigenic effects of ROS, and hence the potential benefit of antioxidants (61, 63–65), recent findings have demonstrated the positive impact of ROS in limiting blood-borne metastasis. In mouse models, systemic injections of the antioxidant N-acetyl-cysteine (NAC) enhance metastatic tumor formation following intravascular inoculation of primary human melanoma cells (17). In an endogenous mouse model of malignant melanoma, *in vivo* administration of NAC or the vitamin E analogue Trolox accelerates tumor progression and lymph node metastasis (66). Similarly, using single-cell RNA-seq of prostate cancer CTCs, we previously noted overexpression of multiple gene signatures involved in antioxidative defense, including β-hemoglobin, whose induction by *KLF4* contributes to blood-borne metastasis (41, 62). While this

work was under revision, Ubellacker and colleagues described a model whereby metastasizing melanoma cells are initially shielded from ferroptosis as they spread through low oxygen tension lymphatic channels, enhancing their subsequent ability to resist ROS stress during subsequent intravascular dissemination (67). Among the mechanisms employed by CTCs to circumvent oxidative stress in the bloodstream, the SREBP2-mediated induction of *TF* constitutes a novel pathway that may provide unique therapeutic opportunities.

In vitro, iron chelation using DFO suppresses ferroptosis, consistent with the iron requirement for lipid peroxidation (68). Altering serum iron levels to increase tumor cell ferroptosis is not feasible; however, inhibitors of lipogenesis may provide an intriguing opportunity to suppress the *SREBP–TF* pathway. Epidemiologic studies have produced conflicting results as to the general effectiveness of statins on cancer outcomes (69–73). These inconsistent clinical findings may reflect the distinct lipogenesis dependencies of different cancer types, interpatient heterogeneity, as well as different timing of drug administration as part of large observational clinical studies. Our results using melanoma CTC models raise the possibility that the short transit of tumor cells through the bloodstream may provide a unique window of opportunity to target these cells at a time of extraordinary ROS stress. As such, targeting the SREBP pathway in the context of melanoma with a high risk for metastatic recurrence may present a potential therapeutic strategy. Taken together, the cross-talk between SREBP and *TF* reveals a new and potentially therapeutically relevant vulnerability of highly refractory metastatic precursor cells.

METHODS

Experimental Mouse Model and Human Subjects

Written informed consent was obtained from patients with metastatic melanoma undergoing evaluation or treatment at the Massachusetts General Hospital Cancer Center, and blood collections (10–15 mL) were performed as per IRB protocol (DF/HCC-0500), in accordance with the U.S. ethical guidelines. CTCs were microfluidically enriched from peripheral blood samples, using high-efficiency negative depletion of hematopoietic cells to isolate untagged and potentially viable cancer cells, as previously described (CTC-iChip; refs. 22, 23). All CTC lines were maintained under anchorage-independent culture condition as described previously (25). Standard melanoma cell lines IGR-37, SKML28, GAK, and A375 were obtained from the ATCC. CTC and ATCC cell lines used in this study have been authenticated using the short tandem repeat profiling method (Genetica) and tested for *Mycoplasma* contamination using a Mycoalert kit (Lonza, catalog no. LT07-218) before experiments. Mouse models of tumorigenesis and metastasis were generated using cultured Mel-167 and Mel-182-2 CTC lines in immunocompromised NOD/SCID *Il2rg*$^{-/-}$ mice, according to guidelines approved by the Massachusetts General Hospital (MGH) Institutional Animal Care and Use committee (IACUC No. 2010N000006).

Plasmid Construction

FLAG-tagged *SREBF2* and *TF* constructs were obtained from Addgene (*SREBF2* #26807 and *TF* #67240) and subcloned into pInducer10 vector using restriction enzymatic digestion (5′ using Age1 and 3′ using Mlu1). Lentiviral shRNAs were purchased from The RNAi Consortium (TRC) shRNA libraries of the Broad Institute. The targeting sequences for *TF* are sh*TF* #1 5-ACTACAATAAGAGCGATAATT-3 and sh*TF* #2 5-TACACCAGAGGCAGGGGTATTT-3.

CTC Ex Vivo Culture

For *ex vivo* culture of melanoma CTCs, microfluidically processed samples were incubated in hypoxic, anchorage-independent conditions as described in Yu and colleagues (25) with modifications. CTC cultures were grown in ultralow attachment plates (Corning) containing tumor sphere medium consisting of RPMI-1640 medium (with phenol red) supplemented with EGF (20 ng/mL), basic FGF (20 ng/mL), B27 (10 mL, 50× in stock), 1× Antibiotic–Antimycotic (Life Technologies), 5 μg/mL Heparin (Stemcell Technologies), and 100 nmol/L Rock inhibitor Y-27632 (EMD Millipore). Cells were cultured in a humid 37°C incubator with 5% CO_2 and 4% O_2. Medium was replenished 2 to 3 times per week, until CTCs initiated *in vitro* proliferation (4–8 weeks) with the following components included in CTC culture media: Mel-182 and Pem-22 blood samples were processed through the CTC-iChip using a recently developed blood stabilization method (74) followed by three-dimensional fibrin Matrigel culture initially and switched to anchorage-independent condition after initial proliferation.

Mouse Xenograft and Metastasis Assays

For primary tumorigenesis assays, NOD/SCID *Il2rg*$^{-/-}$ mice (6–8 weeks old, female) were injected s.c. in the left flank with cultured CTCs, and tumors were harvested when they reached 2 cm in diameter. For metastasis assays, 100,000 to 500,000 cells were injected intravascularly (tail vein or intracardiac). Metastatic burden was monitored 2 to 3 times per week using *in vivo* luciferase imaging using the IVIS (PerkinElmer). Mice were sacrificed at 8 to 10 weeks after tumor cell inoculation or at the first sign of discomfort as per IACUC guidelines.

Soft-Agar Clonogenic Assays

Cultured CTCs were resuspended in growth media containing 0.4% low-melting agarose (Sigma, type VII). Soft agarose (0.5 mL of 1% soft agarose solution) was layered and solidified at room temperature in 24-well plates before adding the cell–agar mixture. Freshly plated cells were incubated at 4°C for 6 minutes to ensure solidification of the soft agar, and 0.5 mL of culture medium was added to each well. Colony formation was assayed after 4 weeks by staining with colorimetric MTT assay. Plates were photographed under identical standardized settings, and colonies were scored using an automated Matlab script.

siRNA and shRNA Knockdown

Melanoma CTCs were seeded in 6-well plates the day before siRNA introduction by Lipofectamine RNAiMAX (Thermo Fisher, catalog no. 13778030) transfection. ON_TARGET plus smart pool siRNA was used to target *SREBF1* (Dharmacon, catalog no. L-006891-00-0005) and *SREBF2* (catalog no. L-009549-00-0005). Growth media were replaced once after 12 hours of transfection, and siRNA knockdown efficiency was assessed by qPCR 48 hours after transfection. shRNAs in lentiviral backbone against *TF* and scramble shRNA control vector were purchased from the TRC shRNA library at Broad Institute. shRNA lentiviruses were produced and packaged in 293T cells as described previously (75). Virus transduction was carried out in CTCs incubated in sealed 6-well plates by centrifugation followed by puromycin (2 μg/mL) selection for 6 to 8 days.

In Vitro Drug Sensitivity Assays

Cultured CTCs were refreshed with growth media in suspension the day before drug exposure and then split into ultralow attachment 96-well plates (Corning Costar-3474) at a density of 1,000 cells per well. Serial dilutions of each drug were added to the media, and cell viability was measured 5 days after drug exposure using CellTiter-Glo2.0 (Promega, catalog no. G9243).

ROS Measurements

Control or *TF*-KD CTCs were incubated with fresh media the day before ROS detection. Cells with 1x ROS fluorescent probe (Abcam, catalog no. ab186029) were incubated at 37°C for 1 hour in CTC growth chamber. ROS quantification was performed using flow cytometry (calculated based on the geometric mean), and relative ROS level was calculated and normalized to control shRNA-treated CTCs.

Lipid Peroxidation Assay

CTC cells were preincubated with fresh media 24 hours before the experiment. Cells were stained with 1x BODIPY 581/591 C11 lipid peroxidation sensor (Invitrogen, catalog no. D3861) for 30 minutes at 37°C. After the incubation, CTCs were washed with PBS and sent for flow cytometry quantification. The fraction of cells positive for oxidized BODIPY 581/591 C11 signal (shifts in emission peaks from 590 to 510 nm upon oxidation) was analyzed and normalized to control shRNA-treated CTCs.

RT-PCR and Western Blot Analyses

RNA was extracted by a column purification kit (QIAGEN RNeasy), followed by treatment with DNAse I and oligo-dT–based reverse transcription using Superscript III. qRT-PCR was performed using SYBR Green reagents on an ABI 7500 fast real-time PCR platform. For immunoblotting, cells were washed once with cold TBS [20 mmol/L Tris-HCl (pH 7.5) and 150 mmol/L NaCl] and lysed using cell lysis buffer containing 1x TBS, 10 mmol/L β-glycerophosphate, 5 mmol/L EGTA, 1 mmol/L $Na_4P_2O_7$, 5 mmol/L NaF, 0.5% Triton X-100, 1 mmol/L Na_3VO_4, 1 mmol/L dithiothreitol, and protease inhibitor cocktail (Roche). Following SDS-PAGE, antibody-tagged proteins were detected using Western Lightning Plus-ECL reagent (Perkin-Elmer) after SDS-PAGE. Primary antibodies used in the experiment are rabbit anti-FLAG (1:1,000; Invitrogen, catalog no. PA1-984B); rabbit anti-*TF* (1:2,000; Invitrogen, catalog no. PA3-913); mouse anti-*TFRC* (1:2,000; Life Technologies, catalog no. 136800), and rabbit anti-GAPDH (1:2,000; Cell Signaling Technology, catalog no. 2118S).

Single-Cell RNA Library Construction and Sequencing

Freshly isolated individual CTCs were selected using a micromanipulator and introduced into a 0.5 mL tube with 7 mL of 1x lysis buffer (Takara, catalog no. 634891) containing recombinant RNase inhibitor (0.4 U/mL; Takara, catalog no. 2313A), snap-frozen, and maintained at −80°C until processing. Single-cell lysates were transferred into 96-well plates (Eppendorf, 951020401), and RNA extraction and cleanup were carried out using Agencourt RNAClean XP Solid Phase Reversible Immobilization beads (Beckman Coulter, A63987). Prior to library construction using the Nextera XT library Prep Kit (Illumina, FC-131-1096), two steps of quality control were done to evaluate the concentration of each single cell, using Qubit dsDNA High Sensitivity Assay Kit (Life Technologies, Q32854), according to the manufacturer's instructions. Single-cell CTC libraries were prepared using a modified Smart-Seq2 protocol (76). Combined libraries were sequenced on a NextSeq 500 sequencer (Illumina) using the 75 cycles kit, with paired-end 38-base reads and dual barcoding.

Computational Analyses

Detailed computational analytic methods can be found in the Supplementary Methods.

Statistical Analysis

Statistical analyses were performed using R 3.5.1. An empirical Bayes moderated *t* test was used for two-group comparison of gene expression values. Two-sided Welch *t* test was used for two-group comparison of GSVA enrichment scores.

Data and Software Availability

All RNA-seq and ChIP-seq data associated with this article are deposited into Gene Expression Omnibus repository with the accession number GSE157745 (https://www.ncbi.nlm.nih.gov/geo/query/acc.cgi?acc=GSE157745). The WES of melanoma CTC lines (as shown in Supplementary Fig. S3A) will be provided upon request.

Authors' Disclosures

X. Hong reports patents for PCT/US2016/024367 and PCT/US2017/058855 issued. R.J. Sullivan reports grants and personal fees from Merck, grants from Amgen, and personal fees from Novartis, Eisai, Iovance, AstraZeneca, Pfizer, Array, Asana Biosciences, Replimune, and Bristol Myers Squibb outside the submitted work. M. Sade-Feldman reports grants from Dr. Miriam and Sheldon G. Adelson Medical Research Foundation during the conduct of the study; in addition, M. Sade Feldman has a patent for Methods for Predicting Outcomes of Checkpoint Inhibition and Treatment Thereof pending. G.M. Boland reports other from Novartis and Nektar Therapeutics, and grants from Olink Proteomics, Palleon Pharmaceuticals, and Takeda Oncology outside the submitted work. S.S. Freeman reports a patent for Methods for Predicting Outcomes of Checkpoint Inhibition and Treatment Thereof pending. N. Hacohen reports personal fees from BioNTech/Neon and Related Sciences outside the submitted work. D.T. Ting reports other from TellBio, Inc., during the conduct of the study; in addition, D.T. Ting also reports personal fees and other from ROME Therapeutics; other from PanTher Therapeutics; personal fees from Third Rock Ventures, Foundation Medicine, Inc., EMD Millipore Sigma, NanoString Technologies, and Pfizer; and grants from PureTech Health and Ribon Therapeutics outside the submitted work. M. Toner has equity in a start-up called TellBio interested in the use of CTCs for both diagnostics and therapeutics. G. Getz reports grants from IBM during the conduct of the study, receives research funds from Pharmacyclics, and is an inventor on patent applications related to ABSOLUTE, MutSig, MSMuTect, MSMutSig, MSIDetect, POLYSOLVER, and TensorQTL, in addition, G. Getz is a founder and consultant and holds privately held equity in Scorpion Therapeutics. S. Maheswaran has equity in TellBio; in addition, S. Maheswaran has a patent for CTC diagnostics pending. D.A. Haber has equity in TellBio; in addition, D.A. Haber has a patent for CTC diagnostics pending. No disclosures were reported by the other authors.

Authors' Contributions

X. Hong: Conceptualization, formal analysis, investigation, writing–original draft. **W. Roh:** Formal analysis, investigation, writing–original draft. **R.J. Sullivan:** Resources, investigation, writing–review and editing. **K.H.K. Wong:** Formal analysis, investigation, writing–review and editing. **B.S. Wittner:** Formal analysis, investigation, writing–original draft. **H. Guo:** Formal analysis, investigation, writing–original draft. **T.D. Dubash:** Formal analysis, investigation, writing–review and editing. **M. Sade-Feldman:** Formal analysis, investigation, writing–review and editing. **B. Wesley:** Formal analysis, investigation, writing–review and editing. **E. Horwitz:** Formal analysis, investigation, writing–review and editing. **G.M. Boland:** Resources, writing–review and editing. **D.L. Marvin:** Formal analysis, investigation, writing–review and editing. **T. Bonesteel:** Formal analysis, investigation, writing–review and editing. **C. Lu:** Formal analysis, investigation, writing–review and editing. **F. Aguet:** Formal analysis, investigation, writing–review and editing. **R. Burr:** Formal analysis, investigation, writing–review and editing. **S.S. Freeman:** Formal analysis, writing–review and editing. **L. Parida:** Investigation, writing–review and editing. **K. Calhoun:** Investigation, writing–review and editing. **M.K. Jewett:** Investigation, writing–review and editing. **L.T. Nieman:** Formal analysis, investigation, writing–review

and editing. **N. Hacohen:** Formal analysis, investigation, writing–original draft. **A.M. Näär:** Resources, formal analysis, writing–review and editing. **D.T. Ting:** Formal analysis, writing–review and editing. **M. Toner:** Formal analysis, supervision, writing–original draft. **S.L. Stott:** Supervision, investigation, writing–original draft. **G. Getz:** Supervision, investigation, writing–original draft. **S. Maheswaran:** Conceptualization, formal analysis, supervision, investigation, writing–original draft. **D.A. Haber:** Conceptualization, formal analysis, supervision, investigation, writing–original draft.

Acknowledgments

The authors thank the patients who participated in this study and L. Libby for administrative support. This work was supported by grants from the National Institutes of Health [2RO1CA129933 (to D.A. Haber), 2U01EB012493 (to M. Toner, D.A. Haber, and S. Maheswaran), 5U01EB012493 (to M. Toner), and 5P41EB002503 (to M. Toner)], Howard Hughes Medical Institute (to D.A. Haber), ESSCO Breast Cancer Research Fund (to S. Maheswaran), National Foundation for Cancer Research (to D.A. Haber), Wang Pediatric Brain Tumor Collaborative and MGH Claflin Distinguished Scholar Award (to S.L. Stott), MGH Research Scholar Award (to A.M. Näär), Broad/IBM Cancer Resistance Research Project (to G. Getz), National Science Foundation (PHY-1549535 to D.T. Ting), Stand Up To Cancer (SU2C; to D.T. Ting), Lustgarten Foundation (2015-002, to D.T. Ting), and ACD_Biotechne (to D.T. Ting).

Received December 18, 2019; revised September 22, 2020; accepted November 12, 2020; published first November 17, 2020.

REFERENCES

1. Chapman PB, Hauschild A, Robert C, Haanen JB, Ascierto P, Larkin J, et al. Improved survival with vemurafenib in melanoma with BRAF V600E mutation. N Engl J Med 2011;364:2507–16.
2. Flaherty KT, Robert C, Hersey P, Nathan P, Garbe C, Milhem M, et al. Improved survival with MEK inhibition in BRAF-mutated melanoma. N Engl J Med 2012;367:107–14.
3. Hauschild A, Grob JJ, Demidov LV, Jouary T, Gutzmer R, Millward M, et al. Dabrafenib in BRAF-mutated metastatic melanoma: a multicentre, open-label, phase 3 randomised controlled trial. Lancet 2012;380:358–65.
4. Hodi FS, O'Day SJ, McDermott DF, Weber RW, Sosman JA, Haanen JB, et al. Improved survival with ipilimumab in patients with metastatic melanoma. N Engl J Med 2010;363:711–23.
5. Robert C, Thomas L, Bondarenko I, O'Day S, Weber J, Garbe C, et al. Ipilimumab plus dacarbazine for previously untreated metastatic melanoma. N Engl J Med 2011;364:2517–26.
6. Robert C, Ribas A, Wolchok JD, Hodi FS, Hamid O, Kefford R, et al. Anti-programmed-death-receptor-1 treatment with pembrolizumab in ipilimumab-refractory advanced melanoma: a randomised dose-comparison cohort of a phase 1 trial. Lancet 2014;384:1109–17.
7. Robert C, Schachter J, Long GV, Arance A, Grob JJ, Mortier L, et al. Pembrolizumab versus ipilimumab in advanced melanoma. N Engl J Med 2015;372:2521–32.
8. Robert C, Long GV, Brady B, Dutriaux C, Maio M, Mortier L, et al. Nivolumab in previously untreated melanoma without BRAF mutation. N Engl J Med 2015;372:320–30.
9. Le DT, Uram JN, Wang H, Bartlett BR, Kemberling H, Eyring AD, et al. PD-1 blockade in tumors with mismatch-repair deficiency. N Engl J Med 2015;372:2509–20.
10. Rizvi NA, Hellmann MD, Snyder A, Kvistborg P, Makarov V, Havel JJ, et al. Cancer immunology. Mutational landscape determines sensitivity to PD-1 blockade in non-small cell lung cancer. Science 2015;348:124–8.
11. Schumacher TN, Schreiber RD. Neoantigens in cancer immunotherapy. Science 2015;348:69–74.
12. Johnson DB, Frampton GM, Rioth MJ, Yusko E, Xu Y, Guo X, et al. Targeted next generation sequencing identifies markers of response to PD-1 blockade. Cancer Immunol Res 2016;4:959–67.
13. Wolf Y, Bartok O, Patkar S, Eli GB, Cohen S, Litchfield K, et al. UVB-induced tumor heterogeneity diminishes immune response in melanoma. Cell 2019;179:219–35.
14. Jimenez-Sanchez A, Memon D, Pourpe S, Veeraraghavan H, Li Y, Vargas HA, et al. Heterogeneous tumor-immune microenvironments among differentially growing metastases in an ovarian cancer patient. Cell 2017;170:927–38.
15. Topalian SL, Sznol M, McDermott DF, Kluger HM, Carvajal RD, Sharfman WH, et al. Survival, durable tumor remission, and long-term safety in patients with advanced melanoma receiving nivolumab. J Clin Oncol 2014;32:1020–30.
16. Schadendorf D, Hodi FS, Robert C, Weber JS, Margolin K, Hamid O, et al. Pooled analysis of long-term survival data from phase II and phase III trials of ipilimumab in unresectable or metastatic melanoma. J Clin Oncol 2015;33:1889–94.
17. Piskounova E, Agathocleous M, Murphy MM, Hu Z, Huddlestun SE, Zhao Z, et al. Oxidative stress inhibits distant metastasis by human melanoma cells. Nature 2015;527:186–91.
18. Yu M, Stott S, Toner M, Maheswaran S, Haber DA. Circulating tumor cells: approaches to isolation and characterization. J Cell Biol 2011;192:373–82.
19. Allard WJ, Matera J, Miller MC, Repollet M, Connelly MC, Rao C, et al. Tumor cells circulate in the peripheral blood of all major carcinomas but not in healthy subjects or patients with nonmalignant diseases. Clin Cancer Res 2004;10:6897–904.
20. Cristofanilli M, Budd GT, Ellis MJ, Stopeck A, Matera J, Miller MC, et al. Circulating tumor cells, disease progression, and survival in metastatic breast cancer. N Engl J Med 2004;351:781–91.
21. Luo X, Mitra D, Sullivan RJ, Wittner BS, Kimura AM, Pan S, et al. Isolation and molecular characterization of circulating melanoma cells. Cell Rep 2014;7:645–53.
22. Ozkumur E, Shah AM, Ciciliano JC, Emmink BL, Miyamoto DT, Brachtel E, et al. Inertial focusing for tumor antigen-dependent and -independent sorting of rare circulating tumor cells. Sci Transl Med 2013;5:179ra47.
23. Karabacak NM, Spuhler PS, Fachin F, Lim EJ, Pai V, Ozkumur E, et al. Microfluidic, marker-free isolation of circulating tumor cells from blood samples. Nat Protoc 2014;9:694–710.
24. Hong X, Sullivan RJ, Kalinich M, Kwan TT, Giobbie-Hurder A, Pan S, et al. Molecular signatures of circulating melanoma cells for monitoring early response to immune checkpoint therapy. Proc Natl Acad Sci U S A 2018;115:2467–72.
25. Yu M, Bardia A, Aceto N, Bersani F, Madden MW, Donaldson MC, et al. Cancer therapy. Ex vivo culture of circulating breast tumor cells for individualized testing of drug susceptibility. Science 2014;345:216–20.
26. Medford AJ, Dubash TD, Juric D, Spring L, Niemierko A, Vidula N, et al. Blood-based monitoring identifies acquired and targetable driver HER2 mutations in endocrine-resistant metastatic breast cancer. NPJ Precis Oncol 2019;3:18.
27. Jordan NV, Bardia A, Wittner BS, Benes C, Ligorio M, Zheng Y, et al. HER2 expression identifies dynamic functional states within circulating breast cancer cells. Nature 2016;537:102–6.
28. Cancer Genome Atlas Network. Genomic classification of cutaneous melanoma. Cell 2015;161:1681–96.
29. Barretina J, Caponigro G, Stransky N, Venkatesan K, Margolin AA, Kim S, et al. The Cancer Cell Line Encyclopedia enables predictive modelling of anticancer drug sensitivity. Nature 2012;483:603–7.
30. Hanzelmann S, Castelo R, Guinney J. GSVA: gene set variation analysis for microarray and RNA-seq data. BMC Bioinformatics 2013;14:7.
31. Toth JI, Datta S, Athanikar JN, Freedman LP, Osborne TF. Selective coactivator interactions in gene activation by SREBP-1a and -1c. Mol Cell Biol 2004;24:8288–300.
32. Chen M, Zhang J, Sampieri K, Clohessy JG, Mendez L, Gonzalez-Billalabeitia E, et al. An aberrant SREBP-dependent lipogenic program promotes metastatic prostate cancer. Nat Genet 2018;50:206–18.

33. Shimano H, Sato R. SREBP-regulated lipid metabolism: convergent physiology-divergent pathophysiology. Nat Rev Endocrinol 2017;13:710–30.
34. Ricoult SJ, Yecies JL, Ben-Sahra I, Manning BD. Oncogenic PI3K and K-Ras stimulate de novo lipid synthesis through mTORC1 and SREBP. Oncogene 2016;35:1250–60.
35. Weirauch MT, Yang A, Albu M, Cote AG, Montenegro-Montero A, Drewe P, et al. Determination and inference of eukaryotic transcription factor sequence specificity. Cell 2014;158:1431–43.
36. Messori L, Kratz F. Transferrin: from inorganic biochemistry to medicine. Met Based Drugs 1994;1:161–7.
37. Shen Y, Li X, Dong D, Zhang B, Xue Y, Shang P. Transferrin receptor 1 in cancer: a new sight for cancer therapy. Am J Cancer Res 2018;8:916–31.
38. Bloch B, Popovici T, Levin MJ, Tuil D, Kahn A. Transferrin gene expression visualized in oligodendrocytes of the rat brain by using in situ hybridization and immunohistochemistry. Proc Natl Acad Sci U S A 1985;82:6706–10.
39. Pascale RM, De Miglio MR, Muroni MR, Simile MM, Daino L, Seddaiu MA, et al. Transferrin and transferrin receptor gene expression and iron uptake in hepatocellular carcinoma in the rat. Hepatology 1998;27:452–61.
40. Aceto N, Bardia A, Miyamoto DT, Donaldson MC, Wittner BS, Spencer JA, et al. Circulating tumor cell clusters are oligoclonal precursors of breast cancer metastasis. Cell 2014;158:1110–22.
41. Miyamoto DT, Zheng Y, Wittner BS, Lee RJ, Zhu H, Broderick KT, et al. RNA-Seq of single prostate CTCs implicates noncanonical Wnt signaling in antiandrogen resistance. Science 2015;349:1351–6.
42. Arosio P, Levi S. Ferritin, iron homeostasis, and oxidative damage. Free Radic Biol Med 2002;33:457–63.
43. Stockwell BR, Friedmann Angeli JP, Bayir H, Bush AI, Conrad M, Dixon SJ, et al. Ferroptosis: a regulated cell death nexus linking metabolism, redox biology, and disease. Cell 2017;171:273–85.
44. Hassannia B, Vandenabeele P, Vanden Berghe T. Targeting ferroptosis to iron out cancer. Cancer Cell 2019;35:830–49.
45. Yang WS, Stockwell BR. Synthetic lethal screening identifies compounds activating iron-dependent, nonapoptotic cell death in oncogenic-RAS-harboring cancer cells. Chem Biol 2008;15:234–45.
46. Hangauer MJ, Viswanathan VS, Ryan MJ, Bole D, Eaton JK, Matov A, et al. Drug-tolerant persister cancer cells are vulnerable to GPX4 inhibition. Nature 2017;551:247–50.
47. Viswanathan VS, Ryan MJ, Dhruv HD, Gill S, Eichhoff OM, Seashore-Ludlow B, et al. Dependency of a therapy-resistant state of cancer cells on a lipid peroxidase pathway. Nature 2017;547:453–7.
48. Holzel M, Bovier A, Tuting T. Plasticity of tumour and immune cells: a source of heterogeneity and a cause for therapy resistance? Nat Rev Cancer 2013;13:365–76.
49. Miyamoto DT, Ting DT, Toner M, Maheswaran S, Haber DA. Single-cell analysis of circulating tumor cells as a window into tumor heterogeneity. Cold Spring Harb Symp Quant Biol 2016;81:269–74.
50. Bao J, Zhu L, Zhu Q, Su J, Liu M, Huang W. SREBP-1 is an independent prognostic marker and promotes invasion and migration in breast cancer. Oncol Lett 2016;12:2409–16.
51. Guo D, Prins RM, Dang J, Kuga D, Iwanami A, Soto H, et al. EGFR signaling through an Akt-SREBP-1-dependent, rapamycin-resistant pathway sensitizes glioblastomas to antilipogenic therapy. Sci Signal 2009;2:ra82.
52. Lee JH, Jeon YG, Lee KH, Lee HW, Park J, Jang H, et al. RNF20 suppresses tumorigenesis by inhibiting the SREBP1c-PTTG1 axis in kidney cancer. Mol Cell Biol 2017;37:e00265–17.
53. Talebi A, Dehairs J, Rambow F, Rogiers A, Nittner D, Derua R, et al. Sustained SREBP-1-dependent lipogenesis as a key mediator of resistance to BRAF-targeted therapy. Nat Commun 2018;9:2500.
54. Guo D, Bell EH, Mischel P, Chakravarti A. Targeting SREBP-1-driven lipid metabolism to treat cancer. Curr Pharm Des 2014;20:2619–26.
55. Horton JD, Shah NA, Warrington JA, Anderson NN, Park SW, Brown MS, et al. Combined analysis of oligonucleotide microarray data from transgenic and knockout mice identifies direct SREBP target genes. Proc Natl Acad Sci U S A 2003;100:12027–32.
56. Wang W, Green M, Choi JE, Gijon M, Kennedy PD, Johnson JK, et al. CD8(+) T cells regulate tumour ferroptosis during cancer immunotherapy. Nature 2019;569:270–4.
57. Rychtarcikova Z, Lettlova S, Tomkova V, Korenkova V, Langerova L, Simonova E, et al. Tumor-initiating cells of breast and prostate origin show alterations in the expression of genes related to iron metabolism. Oncotarget 2017;8:6376–98.
58. Gao M, Monian P, Quadri N, Ramasamy R, Jiang X. Glutaminolysis and transferrin regulate ferroptosis. Mol Cell 2015;59:298–308.
59. Takahashi N, Chen HY, Harris IS, Stover DG, Selfors LM, Bronson RT, et al. Cancer cells co-opt the neuronal redox-sensing channel TRPA1 to promote oxidative-stress tolerance. Cancer Cell 2018;33:985–1003.
60. Tsoi J, Robert L, Paraiso K, Galvan C, Sheu KM, Lay J, et al. Multi-stage differentiation defines melanoma subtypes with differential vulnerability to drug-induced iron-dependent oxidative stress. Cancer Cell 2018;33:890–904.
61. Yun J, Mullarky E, Lu C, Bosch KN, Kavalier A, Rivera K, et al. Vitamin C selectively kills KRAS and BRAF mutant colorectal cancer cells by targeting GAPDH. Science 2015;350:1391–6.
62. Zheng Y, Miyamoto DT, Wittner BS, Sullivan JP, Aceto N, Jordan NV, et al. Expression of beta-globin by cancer cells promotes cell survival during blood-borne dissemination. Nat Commun 2017;8:14344.
63. Irani K, Xia Y, Zweier JL, Sollott SJ, Der CJ, Fearon ER, et al. Mitogenic signaling mediated by oxidants in Ras-transformed fibroblasts. Science 1997;275:1649–52.
64. Chan DW, Liu VW, Tsao GS, Yao KM, Furukawa T, Chan KK, et al. Loss of MKP3 mediated by oxidative stress enhances tumorigenicity and chemoresistance of ovarian cancer cells. Carcinogenesis 2008;29:1742–50.
65. Kumar B, Koul S, Khandrika L, Meacham RB, Koul HK. Oxidative stress is inherent in prostate cancer cells and is required for aggressive phenotype. Cancer Res 2008;68:1777–85.
66. Le Gal K, Ibrahim MX, Wiel C, Sayin VI, Akula MK, Karlsson C, et al. Antioxidants can increase melanoma metastasis in mice. Sci Transl Med 2015;7:308re8.
67. Ubellacker JM, Tasdogan A, Ramesh V, Shen B, Mitchell EC, Martin-Sandoval MS, et al. Lymph protects metastasizing melanoma cells from ferroptosis. Nature 2020;585:113–8.
68. Dixon SJ, Lemberg KM, Lamprecht MR, Skouta R, Zaitsev EM, Gleason CE, et al. Ferroptosis: an iron-dependent form of nonapoptotic cell death. Cell 2012;149:1060–72.
69. Liu B, Yi Z, Guan X, Zeng YX, Ma F. The relationship between statins and breast cancer prognosis varies by statin type and exposure time: a meta-analysis. Breast Cancer Res Treat 2017;164:1–11.
70. Abdel-Rahman O. Statin treatment and outcomes of metastatic pancreatic cancer: a pooled analysis of two phase III studies. Clin Transl Oncol 2019;21:810–6.
71. Lytras T, Nikolopoulos G, Bonovas S. Statins and the risk of colorectal cancer: an updated systematic review and meta-analysis of 40 studies. World J Gastroenterol 2014;20:1858–70.
72. Tsan YT, Lee CH, Ho WC, Lin MH, Wang JD, Chen PC. Statins and the risk of hepatocellular carcinoma in patients with hepatitis C virus infection. J Clin Oncol 2013;31:1514–21.
73. Islam MM, Yang HC, Nguyen PA, Poly TN, Huang CW, Kekade S, et al. Exploring association between statin use and breast cancer risk: an updated meta-analysis. Arch Gynecol Obstet 2017;296:1043–53.
74. Wong KHK, Tessier SN, Miyamoto DT, Miller KL, Bookstaver LD, Carey TR, et al. Whole blood stabilization for the microfluidic isolation and molecular characterization of circulating tumor cells. Nat Commun 2017;8:1733.
75. Moffat J, Grueneberg DA, Yang X, Kim SY, Kloepfer AM, Hinkle G, et al. A lentiviral RNAi library for human and mouse genes applied to an arrayed viral high-content screen. Cell 2006;124:1283–98.
76. Sade-Feldman M, Yizhak K, Bjorgaard SL, Ray JP, de Boer CG, Jenkins RW, et al. Defining T cell states associated with response to checkpoint immunotherapy in melanoma. Cell 2019;176:404.